# Beijing Climate Center Earth System Model version 1 (BCC-ESM1): Model Description and Evaluation of Aerosol Simulations

**Tongwen Wu[1*], Fang Zhang[1], Jie Zhang[1], Weihua Jie[1], Yanwu Zhang[1], Fanghua Wu[1], Laurent Li[1,2], Jinghui Yan[1], Xiaohong Liu[3], Xiao Lu[4], Haiyue Tan[4], Lin Zhang[4], Jun Wang[5], Aixue Hu[6]**

[1]Beijing Climate Center, China Meteorological Administration, Beijing, China

[2]Laboratoire de Météorologie Dynamique, IPSL, CNRS, Sorbonne Université, Ecole Normale Supérieure, Ecole Polytechnique, Paris, France

[3] Texas A&M University, College Station, TX, USA

[4] Laboratory for Climate and Ocean-Atmosphere Studies, Department of Atmospheric and Oceanic Sciences, School of Physics, Peking University, Beijing, China

[5] University of Iowa, Iowa City, IA 52242, USA

[6]National Center for Atmospheric Research, PO Box 3000, Boulder, Colorado 80307-3000, USA

*Correspondence to:* Tongwen Wu (twwu@cma.gov.cn)

Submit to Geosci. Model Dev.

**Revised on Oct. 23, 2019**

**Revised on Dec. 14, 2019**

**Abstract.** BCC-ESM1 is the first version of a fully-coupled Earth System Model with interactive atmospheric chemistry and aerosols developed by the Beijing Climate Center, China Meteorological Administration. Major aerosol species (including sulfate, organic carbon, black carbon, dust and sea salt) and greenhouse gases are interactively simulated with a whole panoply of processes controlling emission, transport, gas-phase chemical reactions, secondary aerosol formation, gravitational settling, dry deposition, and wet scavenging by clouds and precipitation. Effects of aerosols on radiation, cloud, and precipitation are fully treated. The performance of BCC-ESM1 in simulating aerosols and their optical properties is comprehensively evaluated as required by the Aerosol Chemistry Model Intercomparison Project (AerChemMIP), covering the preindustrial mean state and time evolution from 1850 to 2014. The simulated aerosols from BCC-ESM1 are quite coherent with CMIP5-recommended data, in-situ measurements from surface networks (such as IMPROVE in the U.S. and EMEP in Europe), and aircraft observations. A comparison of modeled aerosol optical depth (AOD) at 550 nm with satellite observations retrieved from Moderate Resolution Imaging Spectroradiometer (MODIS) and Multi-angle Imaging SpectroRadiometer (MISR) and surface AOD observations from AErosol RObotic NETwork (AERONET) shows reasonable agreements between simulated and observed AOD. However, BCC-ESM1 shows weaker upward transport of aerosols from the surface to the middle and upper troposphere, likely reflecting the deficiency of representing deep convective transport of chemical species in BCC-ESM1. With an overall good agreement between BCC-ESM1 simulated and observed aerosol properties, it demonstrates a success of the implementation of interactive aerosol and atmospheric chemistry in BCC-ESM1.

## 1. Introduction

Atmosphere is a thin gaseous layer around the Earth, consisting of nitrogen, oxygen and a large number of trace gases including important greenhouse gases (GHG) such as water vapor, tropospheric ozone ($O_3$), carbon dioxide ($CO_2$), methane ($CH_4$), nitrous oxide ($N_2O$), and chloro-fluoro-carbons (CFCs). Besides gaseous components, atmosphere also contains various aerosols, which are important for cloud formation and radiative transfer. Atmospheric trace gases and aerosols are actually interactive components of the climate system. Their inclusion in global climate models (GCMs) is a significant enhancement for most state-of-the-art climate models (Lamarque et al., 2013; Collins et al., 2017). Early attempts in coupling global climate dynamics with atmospheric chemistry can be traced back to late 1970s, when 3D transport of ozone and simple stratospheric chemistry were firstly incorporated into a GCM to simulate global $O_3$ production and transport (e.g., Cunnold et al. 1975; Schlesinger and Mintz 1979). Since mid-1980s, a large number of on-line global climate/chemistry models have been developed to address issues of the Antarctic stratospheric $O_3$ depletion (e.g., Cariolle et al. 1990; Austin et al. 1992; Solomon, 1999), tropospheric $O_3$ and sulfur cycle (e.g., Feichter et al. 1996; Barth et al. 2000), tropospheric aerosol and its interactions with cloud (e.g., Chuang et al. 1997; Lohmann et al. 2000; Ghan and Easter, 2006; Jacobson 2012). Aerosols and chemically reactive gases in the atmosphere exert important influences on global and regional air quality and climate (Collins et al., 2017).

Since 2013, the Beijing Climate Center (BCC), China Meteorological Administration, has continuously developed and updated its fully-coupled GCM, the Beijing Climate Center Climate System Model (BCC-CSM) (Wu et al., 2013; Wu et al., 2014; Wu et al., 2019). BCC-CSM version 1.1 was one of the comprehensive carbon-climate models participating in the phase five of the Coupled Model Intercomparison Project (CMIP5, Taylor et al. 2012). When forced by prescribed historical emissions of $CO_2$ from combustion of fossil fuels and land use change, BCC-CSM1.1 successfully reproduced the trends of observed atmospheric $CO_2$ concentration and global surface air temperature from 1850 to 2005 (Wu et al., 2013). During recent years, BCC-CSM1.1 has been used in numerous investigations on soil organic carbon changes (e.g. Todd-Brown et al., 2014), ocean biogeochemistry changes (e.g. Mora et al., 2013), and carbon-climate feedbacks (e.g. Arora et al., 2013; Hoffman et al., 2014).

BCC-CSM includes main climate-carbon cycle processes (Wu et al., 2013) and the global mean atmospheric $CO_2$ concentration is calculated from a prognostic equation of $CO_2$ budget taking into account global anthropogenic $CO_2$ emissions and interactive land-atmosphere and ocean-atmosphere CO2 exchanges.

In recent years, BCC has put large efforts in developing a global climate-chemistry-aerosol fully-coupled Earth System Model (BCC-ESM1) on the basis of BCC-CSM2 (Wu et al., 2019). The objective is to interactively simulate global aerosols (e.g. sulfate, black carbon, etc.) and main greenhouse gases (e.g. $O_3$, $CH_4$, $N_2O$ and $CO_2$) in the atmosphere and to investigate feedbacks between climate and atmospheric chemistry. BCC-ESM1 is at the point to be publicly released, and it is actively used by BCC for several CMIP6-endorsed research initiatives (Eyring et al. 2016), including the Aerosol Chemistry Model Intercomparison Project (AerChemMIP, Collins et al., 2017) and the Coupled Climate–Carbon Cycle Model Intercomparison Project (C4MIP, Jones et al. 2016).

The purpose of this paper is to evaluate the performance of BCC-ESM1 in simulating aerosols and their optical properties in the 20th century. The description of BCC-ESM1 is presented in Section 2. The experimental protocol is given in Section 3. Section 4 presents the evaluations of aerosol simulations with comparisons to CMIP5-recommended data (Lamarque et al., 2010) and data obtained from both global surface networks and satellite observations. The regional and global characteristics compared to observations and estimates from other studies are analyzed. Simulations of aerosol optical properties in the 20th century are also analyzed in Section 4. Conclusions and discussions are summarized in Section 5. Information about code and data availability is given in Section 6.

## 2. Model description

BCC-ESM1 is an Earth System Model with interactive chemistry and aerosol components, in which the atmospheric component is BCC Atmospheric General Model version 3 (Wu et al., 2019) with interactive atmospheric chemistry (hereafter BCC-AGCM3-Chem), land component BCC Atmosphere and Vegetation Interaction Model version 2.0 (hereafter BCC-AVIM2.0), ocean component Modular Ocean Model version 4 (MOM4)-L40, and sea ice component [sea ice simulator (SIS)]. Different components of BCC-ESM1 are fully coupled and interact with each other through fluxes of momentum,

energy, water, carbon and other tracers at their interfaces. The coupling between the atmosphere and the ocean is done every hour.

The atmospheric component BCC-AGCM3-Chem is able to simulate global atmospheric composition and aerosols from anthropogenic emissions as forcing agents. Its resolution is T42 (approximately 2.8125°×2.8125° transformed spectral grid). The model has 26 levels in a hybrid sigma/pressure vertical coordinate system with the top level at 2.914 hPa. Details of the model physics are described in Wu et al. (2019). The BCC-AGCM3-Chem combines 66 gas-phase chemical species and 13 bulk aerosol compounds as listed in Table 1. Apart from 3 gas-phase species of dimethyl sulfide (DMS), sulfur dioxide ($SO_2$) and ammonia ($NH_3$), the other 63 gas-phase species are the same as those in the "standard version" of MOZART2 (Model for Ozone and Related chemical Tracers, version 2), a global chemical transport model for the troposphere developed by the National Center for Atmospheric Research (NCAR) driven by meteorological fields from either climate models or assimilations of meteorological observations (Horowitz et al., 2003). Advection of all tracers in BCC-AGCM3-Chem is performed through a semi-Lagrangian scheme (Williamson and Rasch, 1989), and vertical diffusion within the boundary layer follows the parameterization of Holtslag and Boville (1993). The gas-phase chemistry of the 63 MOZART2 gas-phase species as listed in Table 1 is treated in the same way as that in the "standard version" of MOZART2 (Horowitz et al., 2003), and there are 33 photolytic reactions and 135 chemical reactions involving 30 dry deposited chemical species and 25 soluble gas-phase species. Dry deposition velocities for the 15 trace gases including $O_3$, carbon monoxide (CO), $CH_4$, formaldehyde ($CH_2O$), acetic acid ($CH_3OOH$), hydrogen peroxide ($H_2O_2$), nitrogen dioxide ($NO_2$), nitric acid ($HNO_3$), polyacrylonitrile (PAN), acetone ($CH_3COCH_3$), peroxyacetic acid ($CH_3COOOH$), acetaldehyde ($CH_3CHO$), methylglyoxal ($CH_3COCHO$), nitric oxid (NO), and pernitric acid ($HNO_4$) are not computed interactively and directly interpolated from MOZART2 climatological monthly mean deposition velocities (https://en.wikipedia.org/wiki/MOZART(model)) which are calculated offline (Bey et al., 2001; Shindell et al., 2008) using a resistance-in-series scheme originally described in Wesely (1989). The dry deposition velocities for the other 15 species including peroxy acetyl nitrate (PAN), methyl nitroacetate (ONIT), organic nitrates (ONITR), ethyl alcohol ($C_2H_5OH$), organic

hydroxiperoxide (POOH), ethyl hydroperoxide ($C_2H_5OOH$), propylhydroperoxide ($C_3H_7OOH$), methylene glycol mono acetate (ROOH), glycolaldehyde (GLYALD), acetol (HYAC), methanol ($CH_3OH$), propanoic acid (MACROOH), isoprene hydroxy hydroperoxide (ISOPOOH), carboxylic acid (XOOH), formaldehyde (HYDRALD), and hydrogen ($H_2$) are calculated using prescribed deposition velocities of $O_3$, CO, $CH_3CHO$, or land surface type and surface temperature following the MOZART2 (Horowitz et al., 2003). Wet removal by in-cloud scavenging for 25 soluble gas-phase species in the "standard version" of MOZART2 uses the parameterization of Giorgi and Chameides (1985) based on their temperature dependent effective Henry's law constants. In-cloud scavenging is proportional to the amount of cloud condensate converted to precipitation, and the loss rate depends on the amount of cloud water, the rate of precipitation formation, and the rate of tracer uptake by the liquid phase water. Other highly soluble species such as $HNO_3$, $H_2O_2$, ONIT, ISOPOOH, MACROOH, XOOH, and lead (Pb-210) are also removed by below-cloud washout as calculated using the formulation of Brasseur et al. (1998). Below-cloud scavenging is proportional to the precipitation flux in each model layer and the loss rate depends on the precipitation rate. Vertical transport of gas tracers and aerosols due to deep convection is not yet included in the present version of BCC-AGCM3-Chem, which process is considered as a part of the deep convection and occurs generally in a small spatial region on a GCM-box with low-resolution (2.8 ٩at.×2.8 ٩on.). Another consideration is that a large uncertainty exists to treat transport of those water-soluble tracers by deep convection. But this effect will be involved in the next version of BCC model.

The BCC-AVIM2.0 is the land model with terrestrial carbon cycle. It is described in details in Li et al. (2019) and includes biophysical, physiological, and soil carbon-nitrogen dynamical processes. The terrestrial carbon cycle operates through a series of biochemical and physiological processes on photosynthesis and respiration of vegetation. Biogenic emissions from vegetation are computed online in BCC-AVIM2.0 following the algorithm of the Model of Emissions of Gases and Aerosols from Nature version 2.1 (MEGAN2.1, Guenther et al., 2012).

The oceanic component of BCC-ESM1 is the Modular Ocean Model version 4 with 40 levels (hereafter MOM4-L40), and the sea ice component Sea Ice Simulator (SIS).

MOM4-L40 uses a tripolar grid of horizontal resolution with 1 º longitude by 1/3 º latitude between 30 ℃S and 30 ℃N ranged to 1 º longitude by 1 º latitude from 60 ℃S and 60 ℃N poleward and 40 z-levels in the vertical. Carbon exchange between the atmosphere and the ocean are calculated online in MOM4-L40 using a biogeochemistry module that is based on the protocols from the Ocean Carbon Cycle Model Intercomparison Project–Phase 2 (OCMIP2, http://www.ipsl.jussieu.fr/OCMIP/phase2/). SIS has the same horizontal resolution as MOM4-L40 and three layers in the vertical, including one layer of snow cover and two layers of equally sized sea ice. Details of oceanic component MOM4-L40 and sea-ice component SIS that are used in BCC-ESM1 may be found in Wu et al. (2013) and Wu et al. (2019).

In the following sub-sections, we will describe the treatments in BCC-ESM1 for 3 gas-phase species of DMS, $SO_2$ and $NH_3$, 13 prognostic aerosol species including sulfate ($SO_4^{2-}$), 2 types of organic carbon (hydrophobic OC1, hydrophilic OC2), 2 types of black carbon (hydrophobic BC1, hydrophilic BC2), 4 categories of soil dust (DST01, DST02, DST03, DST04), and 4 categories of sea salt (SSLT01, SSLT02, SSLT03, SSLT04). Concentrations of all aerosols in BCC-ESM1 are mainly determined by advective transport, emission, dry deposition, gravitational settling, and wet scavenging by clouds and precipitation, except for $SO_4^{2-}$ which gas-phase and aqueous phase conversion from $SO_2$ are also considered. The present version of aerosol scheme belongs to a bulk aerosol model and mainly refers to the scheme of CAM-Chem (Lamarque et al., 2012), but the nucleation and coagulation of aerosols are still ignored.

### 2.1 $SO_2$, DMS, $NH_3$, and Sulfate

$SO_2$ is a main sulfuric acid precursor to form aerosol sulfate $SO_4^{2-}$. Conversions of $SO_2$ to $SO_4^{2-}$ occur by gas phase reactions (Table 2) and by aqueous phase reactions in cloud droplets. The dry deposition velocity of $SO_2$ follows the resistance-in-series approach of Wesely (1989) using the formula, $W_{SO2} = 1/(r_a + r_b + r_c)$, in which $r_a$, $r_b$, *and* $r_c$ are the aerodynamic resistance, the quasi-laminar boundary layer resistance, and the surface resistance, respectively and they are interactively computed in each model time step. The loss rate of $SO_2$ due to wet deposition is computed following the scheme in the global Community Atmosphere Model (CAM) version 4, the atmospheric component of the Community Earth System Model (Lamarque et al., 2012).

The sources of $SO_2$ mainly come from fuel combustion, industrial activities, and volcanoes. $SO_2$ can also be formed from the oxidation of DMS as listed in Table 2 in which their reaction rates follow CAM-Chem (Lamarque et al. 2012). The main source of DMS is from oceanic emissions via biogenic processes. It is prescribed with the climatological monthly data that are extracted from MOZART2 package (https://www2.acom.ucar.edu/gcm/mozart-4). $SO_4^{2-}$ is one of the prognostic aerosols in BCC-AGCM3-Chem. Its treatment follows CAM4-Chem (Lamarque et al., 2012). It is produced primarily by the gas-phase oxidation of $SO_2$ (in Table 2) and by aqueous phase oxidation of $SO_2$ in cloud droplets. The gas phase reactions, rate constants, and gas-aqueous equilibrium constants are given by Tie et al. (2001). The heterogeneous reactions of $SO_4^{2-}$ occur on all aerosol surfaces. Their treatment follows a Bulk Aerosol Model (BAM) used in CAM4 (Neale et al., 2010). The heterogeneous reactions depend strongly on pH values in clouds which are calculated from the concentrations of $SO_2$, $HNO_3$, $H_2O_2$, $NH_3$, $O_3$, $HO_2$, and $SO_4^{2-}$. $NH_3$ is a gas tracer apart from MOZART2 (Table 1). Its sources include aircraft and surface emissions due to anthropogenic activity, biomass burning, and biogenic emissions from land soil and ocean surfaces (Table 4). $SO_4^{2-}$ is assumed to be all in aqueous phase due to water uptake, although Wang et al. (2008a) showed that ~34% of sulfate particles are in solid phase globally due to the hysteresis effect of ammonium sulfate phase transition. However, in terms of radiative forcing, consideration of solid sulfate formation process lowers the sulfate forcing by ~8% as compared to consideration of all sulfate particles in aqueous phase (Wang et al., 2008b). Future model development may consider the life cycle of $NH_3$. The sulfate in- and below-cloud scavenging follows Neu and Prather (2011). Washout of $SO_4^{2-}$ is set to 20% of the washout rate of $HNO_3$ following Tie et al. (2005) and Horowitz (2006). Dry deposition velocity of $SO_4^{2-}$ is also calculated by the resistance-in-series approach.

**2.2 Aerosols of organic carbon and black carbon**

BCC-AGCM3-Chem treats two types of organic carbon (OC), i.e. water-insoluble tracer OC1 and water-soluble tracer OC2, and two types of black carbon (BC), i.e. water-insoluble tracer BC1 and water-soluble tracer BC2. As shown in Table 2, hydrophobic BC1 and OC1 can be converted to hydrophilic BC2 and OC2 with a constant rate of $7.1\times10^{-6}$ $s^{-1}$ (Cooke and

Wilson, 1996). The 4 tracers of organic carbon and black carbon are mainly from emissions including both fossil fuel and biomass burning, and are from the CMIP6 data package (https://esgf-node.llnl.gov/search/input4mips/, Hoesly et al., 2018). Beside anthropogenic and biomass burning emissions, hydrophilic organic carbon OC2 can also come from natural biogenic volatile organic compound (VOC) emissions. Dry deposition velocities for all the 4 OC and BC tracers are set to 0.001m.s$^{-1}$. OC2 and BC2 are soluble aerosols, and their sinks are primarily governed by wet deposition. Their in- and below-cloud scavenging follows the scheme of Neu and Prather (2011).

**2.3 Sea salt aerosols**

As shown in Table 3, sea salt aerosols in the model are classified into four size bins (0.2–1.0, 1.0–3.0, 3.0–10, and 10–20 μm) in diameter. They originate from oceans and are calculated online by BCC-ESM1. The upward flux $F_{sea-salt}$ of sea salt productions for four bins is proportional to the 3.41 power of the wind speed $u_{10m}$ at 10 m height near the sea surface (Mahowald et al., 2006) and is expressed as

$$F_{sea-salt} = S \cdot (u_{10m})^{3.41}, \quad (1)$$

where $S$ is a scaling factor and set to 4.05x10$^{-15}$, 4.52x10$^{-14}$, 1.15x10$^{-13}$, 1.20x10$^{-13}$ for four size bins of sea salt aerosols in BCC-ESM1, respectively.

Dry deposition of sea salts depends on the turbulent deposition velocity in the lowest atmospheric layer using aerodynamic resistance and the friction velocity, and the settling velocity through the whole atmospheric column for each bin of sea salts. The turbulent deposition velocity and settling velocity depend on particle diameter and density (listed in Table 3). In addition, the fact that the size of sea salts changes with humidity is also considered. The wet deposition of sea salts follows the scheme for soluble aerosols used in CAM4, and depends on prescribed solubility and size-independent scavenging coefficients.

**2.4 Dust aerosols**

Dust aerosols behave in a similar way as sea salts. Their variations involve three major processes: emission, advective transport, and wet/dry depositions. The dust emission is based on a saltation-sandblasting process, and depends on wind friction velocity, soil moisture, and vegetation/snow cover (Zender et al., 2003). The vertical flux of dust emission is corrected by a surface erodible factor at each model grid cell which has been downloaded from NCAR

website (https://svn-ccsm-inputdata.cgd.ucar.edu/trunk/inputdata/atm/cam/dst/). Soil erodibility is prescribed by a physically-based geomorphic index that is proportional to the runoff area upstream of each source region (Albani et al., 2014). Like sea salts, dry deposition of dust aerosols includes gravitational and turbulent deposition processes, while wet deposition results from both convective and large scale precipitation and is dependent on prescribed size-independent scavenging coefficients.

**2.5 Effects of aerosols on radiation, clouds, and precipitation**

The mass mixing ratios of bulk aerosols are prognostic variables in BCC-ESM1 and directly affect the radiative transfer in the atmosphere with their treatments following the NCAR Community Atmosphere Model (CAM3, Collins et al., 2004). Indirect effects of aerosols are taken into account in the present version of BCC-AGCM3-Chem (Wu et al., 2019). Aerosol particles act as cloud condensation nuclei and exert influence on cloud properties and precipitation, and ultimately impact the hydrological cycle. Prognostic aerosol masses are used to estimate the liquid cloud droplet number concentration $N_{\mathrm{cdnc}}$ ($cm^{-3}$) in BCC-AGCM3-Chem. $N_{\mathrm{cdnc}}$ is explicitly calculated using the empirical function suggested by Boucher and Lohmann (1995) and Quaas et al. (2006):

$$N_{cdnc} = \exp\left[5.1 + 0.41\ln\left(m_{aero}\right)\right] \tag{2}$$

where $m_{\mathrm{aero}}$ ($\mu g.m^{-3}$) is the total mass of all hydrophilic aerosols,

$$m_{aero} = m_{SS} + m_{OC} + m_{SO_4} + m_{NH_4NO_2}, \tag{3}$$

i.e. the first bin of sea salt ($m_{SS}$), hydrophilic organic carbon ($m_{OC}$), sulphate ($m_{SO_4}$), and Ammonium nitrite ($NH_4NO_2$). A dataset of $NH_4NO_2$ from NCAR CAM-Chem (Lamarque et al., 2012) is used in our model.

$N_{\mathrm{cdnc}}$ is an important factor in determining the effective radius of cloud droplets for radiative calculation. The effective radius of cloud droplets $r_{el}$ is estimated as

$$r_{el} = \beta \cdot r_{l,vol}, \tag{4}$$

where $\beta$ is a parameter dependent on the droplets spectral shape and follows the calculation proposed by Peng and Lohmann (2003),

$$\beta = 0.00084 N_{cdnc} + 1.22. \tag{5}$$

288 $r_{l,vol}$ is the volume-weighted mean cloud droplet radius,

289 $$r_{l,vol} = \left[ (3LWC) / (4\pi\rho_w N_{cdnc}) \right]^{1/3}, \quad (6)$$

290 where $\rho_w$ is the liquid water density and $LWC$ the cloud liquid water content (g cm$^{-3}$).

291 Aerosols also exert impacts on precipitation efficiency (Albrecht, 1989), which is taken
292 into account in the parameterization of non-convective cloud processes. There are five
293 processes that convert condensate to precipitate: auto-conversion of liquid water to rain,
294 collection of cloud water by rain, auto-conversion of ice to snow, collection of ice by snow,
295 and collection of liquid by snow. The auto-conversion of cloud liquid water to rain (*PWAUT*)
296 is dependent on the cloud droplet number concentration and follows a formula that was
297 originally suggested by Chen and Cotton (1987),

298 $$PWAUT = C_{l,aut} q_l^2 \rho_a / \rho_w \left( \frac{q_l \rho_a}{\rho_w N_{ncdc}} \right)^{1/3} H\left( r_{l,vol} - r_{lc,vol} \right) \quad (7)$$

299 Where $\hat{q}_l$ is in-cloud liquid water mixing ratio, $\rho_a$ and $\rho_w$ are the local densities of air and
300 water respectively, and $C_{l,aut}$ is a constant. $H(x)$ is the Heaviside step function with the
301 definition,

302 $$H(x) = \begin{cases} 0, & x < 0 \\ 1, & x \geq 0 \end{cases}. \quad (8)$$

303 $r_{lc,vol}$ is the critical value of mean volume radius of liquid cloud droplets $r_{l,vol}$, and set to 15
304 μ m.

305 The treatment of aerosol single scattering (optical) properties (such as mass extinction
306 efficiency, single scattering albedo, and asymmetric factor) follows the look-up table
307 approach in CAM (Collins et al., 2004). The optics for black, organic carbon, sea salt, and sea
308 salt particles is assumed to be same as the optics for soot and water-soluble aerosols in the
309 Optical Properties of Aerosols and Clouds (OPAC) data set (Hess et al., 1998). The optics for
310 dust is derived by Mie calculations for the size distribution represented by each size bin
311 (Zender et al., 2003). Similarly, for sulfate and nitrate particles, same set of aerosol optical
312 properties for ammonium sulfate are used and are taken from Wang et al. (2008b) with
313 treatment of aerosol hygroscopicity. The volcanic stratospheric aerosols are assumed to be
314 comprised of 75% sulfuric acid and 25% water, as in Hess et al. (1998). For each model year,

different aerosol types are assumed to be externally mixed in the calculation of bulk aerosol single scattering properties that are in turn used in the radiative transfer calculations.

## 3. Experiment design for the 20$^{th}$ century climate simulation

There is an Aerosol Chemistry Model Intercomparison Project (AerChemMIP, Collins et al., 2017) endorsed by the Coupled-Model Intercomparison Project 6 (CMIP6) for documenting and understanding past and future changes in the chemical composition of the atmosphere, and estimating the global-to-regional climate response from these changes. Modelling groups with full chemistry and aerosol models are encouraged to perform all AerChemMIP simulations (Collins et al., 2017). To assess the ability of our model to simulate aerosols (mean and variability), we have followed the historical simulation designed by CMIP6 (Eyring et al., 2016) which is named as "historical" experiment in the Earth System Grid Federation (ESGF). The historical experiment is forced with emissions evolving from 1850 to 2014 that include biomass burning emissions (Van Marle et al. 2017), anthropogenic and open burning emissions (Hoesly et al., 2018; Feng et al., 2019). $O_3$ in the historical simulation is an interactive prognostic variable and feedbacks on radiation, and the concentrations of other WMGHG, e.g. $CH_4$, $N_2O$, $CO_2$, CFC11, and CFC12 are prescribed using CMIP6 historical forcing data (Meinshausen et al., 2017). Although $CH_4$ and $N_2O$ are prognostic variables in the chemistry scheme (Table 1), their prognostic values at each model step in the historical experiment are replaced by CMIP6 data (Meinshausen et al., 2017) throughout the model domain. The rest of historical forcing data include: (1) yearly global gridded land-use forcing data sets (Hurtt et al., 2011; Hurtt et al., 2017), and (2) solar forcing (Matthes et al., 2017). All these datasets were downloaded from https://esgf-node.llnl.gov/search/input4mips/. Climate feedback processes that involve changes to the atmospheric composition of reactive gases and aerosols may affect the temperature response to a given WMGHG concentration level.

### 3.1 Surface emissions

Surface emissions of chemical species from different sources are summarized in Table 4. They include anthropogenic emissions from fossil fuel burning and other industrial activities, biomass burning (including vegetation fires, fuel wood and agricultural burning), biogenic emissions from vegetation and soils, and oceanic emissions. Most historical

emissions from anthropogenic source (surface, aircraft plus ship) and biomass burning from 1850 to 2014 are CMIP6-recommended data (available at https://esgf-node.llnl.gov/search/input4mips). Anthropogenic or biomass burning sources of some tracers which are not included in the CMIP6 dataset (see Table 4), anthropogenic emission of $H_2$ and $N_2O$ are from monthly climatological dataset provided by the MOZART-2 standard package. $N_2O$ is a prognostic variable in BCC-ESM1 but it is replaced by CMIP6 prescribed concentration in the historical run. Other emissions including biomass burning ($CH_3COCH_3$) and anthropogenic emission ($CH_3CHO$, $CH_3OH$, and $CH_3COCH_3$) are from the Atmospheric Chemistry and Climate Model Intercomparison Project (ACCMIP) emission inventory (http://accent.aero.jussieu.fr/ACCMIP.php) covering the period from 1850 to 2010 with 10-year intervals (see Table 4). Monthly lumped emissions of black carbon and organic carbon aerosols from 1850 to 2014 are downloaded from CMIP6-recommended data, but we used 80% (for BC) and 50% (for OC) of them in their hydrophobic forms (BC1 and OC1) and the rest in their hydrophilic forms (BC2 and OC2), following the work of Chin et al. (2002).

Five tracers of ISOP, ACET ($CH_3COCH_3$), $C_2H_4$, $C_3H_8$, and Monoterpenes ($C_{10}H_{16}$) in Table 1 belong to biogenic volatile organic carbons (VOCs). As shown in Table 4, those VOCs emissions are online calculated in BCC-ESM1 following the modeling framework of the Model of Emissions of Gases and Aerosols from Nature version 2.1 (MEGAN2.1, Guenther et al., 2012) using simple mechanistic algorithms to account for major known processes controlling biogenic emissions. The MEGAN2.1 can provide a flexible scheme for estimating 16 tracers of biogenic emissions from terrestrial ecosystems including five VOCs emissions used in BCC-ESM1 (Table 4). All the VOCs emissions depend on current and past surface air temperature, solar flux, and the landscape types. Their calculation requires global maps of plant functional type (PFT) and leaf area index (LAI) which is a prognostic variable from the land model BCC-AVIM2. The effect of atmospheric $CO_2$ concentration on isoprene emissions is included. 10% of the biogenic monoterpenes emissions as calculated online with the MEGAN2.1 algorithm in BCC-AVIM2 are converted to hydrophilic organic carbon (OC2) to account for formation of secondary organic aerosols following Chin et al. (2002) in this version of BCC-ESM1.

### 3.2 Volcanic eruptions, lightning and aircraft emissions

As there is no stratospheric aerosol scheme in BCC-ESM1, concentrations of sulfate aerosol at heights from 5 to 39.5 km, which volcanic origin, are directly prescribed using the CMIP6-recommended data (Thomasson et al., 2018) from 1850 to 2014. The effects of surface $SO_2$ emissions from volcanic eruption on the variation of SO2 in the atmosphere and then on the variation of tropospheric $SO_4^{2-}$ concentration are considered, and the $SO_2$ emissions from 1850 to 2014 are downloaded from the IPCC ACCMIP emission inventory (http://accent.aero.jussieu.fr/ACCMIP.php). Aircraft emissions are provided for $NO_2$, CO, $CH_4$, $NH_3$, NO, $SO_2$, and aerosols of OC and BC (Table 1). The emissions of NO from lightning are online calculated in BCC-AGCM3-Chem following the parameterization in MOZART2, and the globally-averaged mean during the period of 1850 to 2014 is 5.19 Tg(N) $yr^{-1}$, which is in agreement with observations within the range of 3 to 6 Tg(N) $yr^{-1}$ (Martin et al., 2002). The lightning frequency depends strongly on the convective cloud top height, and the ratio of cloud-to-cloud versus cloud-to-ground lightning depends on the cold cloud thickness from the level of 0℃ to the cloud top (Price and Rind, 1992).

### 3.3 Upper boundary of the atmosphere

As no stratospheric chemistry is included in the present version of BCC-AGCM3-Chem, it is necessary to ensure a proper distribution of chemically-active stratospheric species. Concentrations of different tracers ($O_3$, $CH_4$, $N_2O$, NO, $NO_2$, $HNO_3$, CO, and $N_2O_5$) at the top two layers of the model are set to prescribed monthly climatological values, and concentrations from below the top two layers to the tropopause are relaxed at a relaxation time of 10-days towards the climatology. Climatological values of NO, $NO_2$, $HNO_3$, CO and $N_2O_5$ at the top two layers are extracted from MOZART2 data package available at the Website (https://www2.acom.ucar.edu/gcm/mozart-4), originated from the Study of Transport and Chemical Reactions in the Stratosphere (STARS, Brasseur et al., 1997). Concentrations for the other tracers ($O_3$, $CH_4$, and $N_2O$) at the top two model layers are the zonally-averaged and monthly values from 1850 to 2014 derived from the CMIP6 data package.

### 3.4 The preindustrial model states

The preindustrial state of BCC-ESM1 is obtained from a piControl simulation of over 600 years in which all forcings including emissions data are fixed at 1850 conditions. The initial state of the piControl simulation itself is obtained through individual spin-up runs of each

component of BCC-ESM1 in order for the piControl simulation to run stably and fast to reach its equilibrium. Figures 1(a-c) show the time series of global yearly means of the net energy budget at top of the atmosphere (TOA), near-surface air temperature (TAS), and sea surface temperature (SST) from the piControl simulation for the last 450 years. It shows that the surface climate in BCC-ESM1 nearly reaches its equilibrium after 600 years piControl simulation. The whole system in BCC-ESM1 fluctuates around +0.7 $Wm^{-2}$ net energy flux at TOA without obvious trend in 450 years (Fig. 1a). This level of TOA energy imbalance is close to the average imbalance (1.0 $Wm^{-2}$) among CMIP5 models (Wild et al., 2013). It means that there exists surplus energy of +0.7 $Wm^{-2}$ obtained by the whole system in BCC-ESM1, but do not cause remarkable climate drift. The global mean TAS and SST keep around 288.1 K (Fig. 1b) and 295.05 K (Fig. 1c), respectively. During the last 450 years, there are ($\pm$0.2 ℃ amplitude of TAS and SST) oscillations of centennial scale for the whole globe (Figs. 1b and 1c), which are certainly caused by internal variation of the system.

Figures 2a-2c show the time series of global annual total burdens of $SO_2$, DMS, and OH in the troposphere (integrated from the surface to 100 hPa) in the last 450 years of the piControl simulation. Without any anthropogenic source, the $SO_2$ amount in the troposphere nearly keeps the level of 0.0868 Tg in the 450 years of the piControl simulation. Tropospheric DMS varies around the value of 0.116 Tg. Tropospheric OH, as an important gas species oxidizing $SO_2$ to form $SO_4^{2-}$ (Table 2), keeps at a stable level in the atmosphere. $SO_4^{2-}$ also remains at a stable level of 0.556 Tg in the atmosphere in the whole period of the piControl simulation (Figure 2d). The amounts of BC and OC in the troposphere vary around 0.0395 Tg and 0.275 Tg (Figures 2e-2f), respectively. Dust and sea salt aerosols are at the level of 22 Tg and 11.7 Tg (Figures 2g-2h), respectively. All those data are close to the global mean concentrations of 0.604 Tg $SO_4^{2-}$, 0.046 Tg BC, 0.30 Tg OC, 22.18 Tg dust, and 11.73 Tg sea salts in 1850 which are estimated based on the CMIP5 prescribed data in 1850 (Lamarque et al., 2010).

Figure 3 shows the global spatial distributions of annual mean sulfate, organic carbon, black carbon, dust, and sea salt aerosols in the whole atmospheric column averaged for the last 100 years of the piControl simulation of BCC-ESM. We can compare them with CMIP5 recommended concentrations in year 1850, considered as the reference state in the

pre-industrial stage. At that time, there are fewer anthropogenic/biomass $SO_2$ emissions, the $SO_4^{2-}$ over land are evidently smaller than those over oceans especially over the tropical Pacific and Atlantic Oceans, where DMS can be oxidized to $SO_2$ and then form $SO_4^{2-}$. There are several centers of high values of black carbon and organic carbon in East and South Asia, Europe, Southeast America, and in the tropical rain forests in Africa and South America. They mainly result from biomass burning including vegetation fires, fuel wood and agricultural burning. Dust aerosols are mainly distributed in North Africa, Central Asia, North China, and Australia, where arid and semi-arid areas locate. Dust emitted from Sahara Desert can be transported to the tropical Atlantic by easterly wind. The sea salt aerosols are mainly distributed over the mid-latitude Southern Oceans, the tropical southern Indian Ocean, and the tropical northern Pacific Ocean, where wind speeds near the sea surface are strong. As shown in Fig. 3, all the spatial distribution patterns of CMIP5-derived sulfate, black carbon, organic carbon, dust, and sea salt aerosols (Lamarque et al., 2010) are well simulated in BCC-ESM1. There are high spatial correlation coefficients, 0.76 for sulfate, 0.77 for black carbon, 0.77 for organic carbon, 0.94 for dust, and 0.94 for sea salts, between CMIP5 data and BCC-ESM1 simulations. Relative lower relations for sulfate, black carbon and organic carbon are possibly caused as different anthropogenic emission sources are used in BCC-ESM1 and to create CMIP5 data. Dust and sea salts belong to natural aerosols and depend on the land and sea surface conditions, so their spatial distributions are easy to be captured and have relatively higher correlations between CMIP5 data and BCC-ESM1 simulations.

## 4. Evaluation of $O_3$ and aerosol simulations in the 20$^{th}$ century

The rate of sulfate formation is dependent on the levels of oxidants in the troposphere. $O_3$ is an important oxidant. So, the evaluation of simulated tropospheric $O_3$ is helpful to understand the aerosols simulations. BCC-ESM1 is driven by most of the CMIP6-recommended emission data. As shown in Figure 4, the zonal distributions of the total amounts of tropospheric $O_3$ below 300 hPa to the ground and their changes with time from 1850 to 2014 from the CMIP6-recommend dataset (Table 4) are well simulated by BCC-ESM1. Evident increasing trends since 1850 almost exist in every latitudes, especially in the Northern Hemisphere where the contents of tropospheric $O_3$ are higher than those in the

Southern Hemisphere.

Figure 5 shows the vertical profiles of $O_3$ simulations with comparison to global ozonesonde observations averaged for the monthly data over 2010-2014 from the World Ozone and Ultraviolet Radiation Data Centre (WOUDC; http://woudc.org/data.php, last access: 24 September 2019) in nine regions which are averaged from 41 global WOUDC sites. The details of WOUDC data may refer to Lu et al. (2019). As shown in Figure 5, BCC-ESM1 well captures the observed ozone vertical structure at all regions. At the lower and middle troposphere (i.e. below 6 km), the model typically shows positive bias within 5 ppbv for the Southern Hemisphere and 10 ppbv for the Northern mid-latitudes, similar to those simulated from many other global atmospheric chemical models (Young et al., 2013, 2018). The model has larger ozone overestimation in the upper troposphere and stratosphere at most regions, at least partly due to the use of prescribed stratospheric ozone as upper boundary conditions and/or errors in modeling ozone exchange between the stratosphere and the troposphere. Global tropospheric ozone burden derived from our simulation is 335 Tg averaged over 2010-2014, in consistent with recent assessment from multi chemistry models (Young et al., 2018).

### 4.1 Global aerosols trends

Figure 6(a)-(c) show the time series of global total emissions of $SO_2$, OC, and BC to the atmosphere from natural and anthropogenic sources. Emissions of $SO_2$ are largely due to industrial production. From 1850 to 1915, $SO_2$ emissions increased year by year as the Industrial Revolution intensified and expanded. But from 1915 to 1945, the increase trend of $SO_2$ emissions became slower as broke out the First and the Second World Wars. After that period, with growing industrial productions, $SO_2$ emissions increased again and reached a maximum around the end of 1970s. During the 1980s and 2000s, with a substantial decrease of $SO_2$ emissions in Europe and the United States, the global $SO_2$ emissions has been decreasing since the 1980s despite the rapid increase of $SO_2$ emissions in South and East Asia as well as in developing countries in the Southern Hemisphere in recent years (Liu et al., 2009). The OC and BC emissions substantially increased since 1950s just after the Second World War. The global total OC emission in 2010 was nearly twice as much as that in pre-industrial (year 1850) and increased by 18 Tg • $yr^{-1}$. Anthropogenic black carbon

emissions increased from 1 Tg $yr^{-1}$ in 1850 to nearly 8 Tg $yr^{-1}$ in 2010.

Anthropogenic $SO_2$, OC and BC emissions strongly affect the variations of atmospheric concentrations of sulfate, OC, and BC. The global $0.5^o x 0.5^o$ gridded data of CMIP5-recommended aerosols masses with 10-years interval from 1850 to 2000 (Lamarque et al., 2010) provides an important reference to evaluate the aerosol simulations in BCC-ESM1. As shown in Figure 7b-7f, the annual total aerosol burdens of $SO_4^{2-}$, OC, and BC in the whole atmosphere column as simulated by the BCC-ESM1 $20^{th}$ century historical simulation are generally consistent with the values derived from CMIP5-recommended aerosols concentrations. Due to increasing $SO_2$ emissions from 1850 to present day (Fig. 6), the global $SO_2$ burden in the atmosphere increased from 100 Tg in 1850s to 200 Tg in 1980s (Fig. 7a), and has a high correlation coefficient of 0.996 with the anthropogenic emissions (Fig. 6a), as the lifetime of $SO_2$ is short. The burden directly followed the emission. DMS in the atmosphere is oxidized by OH and $NO_3$ to form $SO_2$ (Table 2). Its natural emissions from oceans from 1850 to 2010 in the model are the climatological monthly means (Dentener et al., 2006) from MOZART2 data package. As shown in Fig 7a, the global amount of DMS in the whole atmosphere was about 0.12 Tg during 1850-1900 and decreased to 0.055 Tg in 2010. This decrease trend maybe partly results from the speeded rate of DMS oxidation with global warming, and the loss of DMS gradually exceeds the source of ocean DMS emission to cause a net loss of DMS in the atmosphere since 1910s. Largely driven by $SO_2$ anthropogenic emissions, the sulfate burden shows three different stages from 1850 to present. In the first period from 1850s to 1900s, the sulfate burden had a weak linear increase. It increased significantly in the second stage from 1910's to 1940's, and then exploded since 1950's, until the middle 1970s and early 1980s. The sulfate burden then remained nearly stable and even showed slightly decreases as seen from the CMIP5 data. As for global BC and OC burdens, BCC-ESM1 results show continuous increases since 1850s, especially from 1950 to present. From 1910's to 1940's, the CMIP5 data show a slight decrease of BC and OC burdens in the atmosphere.

The dust and sea salt aerosols in the atmosphere are largely determined by the atmospheric circulations and states of the land and ocean surface. We can see that the global dust burden in the atmosphere showed evident increase from 1980 to 2000, which could be

partly caused by evident global warming since 1980 and increasing soil dryness resulting in more surface dust to be released in the atmosphere. Their details will be explored in the other paper.

### 4.2 Global aerosols budgets

We further evaluate global aerosols budgets by comparing a 10-year average of BCC-ESM results from 1990 to 2000 with various studies for sulfate, BC, OC, sea salt, and dust. Their annual total emissions, average atmospheric mass loading, and mean lifetimes are listed in Tables 5 and 6. It is worth emphasizing that the global mean total source and sink for each type of aerosols in BCC-ESM1 are almost balanced.

The global DMS emission from the ocean is 27.4 Tg(S) $yr^{-1}$ in BCC-ESM. This emission in BCC-ESM is nearly balanced by the gas-phase oxidation of DMS to form $SO_2$. The DMS burden is 0.12 Tg with a lifetime of 0.78 days, which is within the range of other models reported in the literature. As shown in Table 5, the total $SO_2$ production averaged for the period of 1991 to 2000 is 76.93 Tg(S) $yr^{-1}$. A rate of 13.2 Tg(S) $yr^{-1}$ (about 17%) $SO_2$ is produced from the DMS oxidation, only 0.1 Tg(S) $yr^{-1}$ $SO_2$ from airplane emissions to the atmosphere, and the rest (63.63 Tg(S) $yr^{-1}$, near 82.7%) from anthropogenic activities and volcanic eruption at surface. The amount of $SO_2$ produced from the DMS oxidation is in the range of other works (10.0 to 24.7 Tg(S) $yr^{-1}$) reported in Liu et al (2005). All the $SO_2$ production is balanced by $SO_2$ losses by dry and wet deposition, and by gas- and aqueous-phase oxidation. Half of its loss (38.74 Tg(S) $yr^{-1}$) occurs via its aqueous-phase oxidation to form sulfate. Other losses through dry and wet depositions and gas-phase oxidation to form $SO_4^{2-}$ are also important (Table 2). All the sinks are in the range from the literature (Liu et al., 2005). The global burden of $SO_2$ in the atmosphere is 0.48 Tg with a lifetime of 1.12 days, consistent with values in literature (Liu et al., 2005).

Sulfate aerosol is mainly produced from aqueous-phase $SO_2$ oxidation (38.73 Tg(S) $yr^{-1}$) and partly from gaseous phase oxidation of $SO_2$ (10.32 Tg(S) $yr^{-1}$), and is largely lost by wet scavenging (49.06 Tg(S) $y^{r-1}$). The total $SO_4^{2-}$ production in BCC-ESM is at the lower range of values in other models reported in Textor et al. (2006). Its global burden is 1.89 Tg and the lifetime is 4.69 days, which are within the range of 1.71 to 2.43 Tg and 3.3 to 5.4 days in the literatures (Textor et al., 2006; Liu et al., 2012; Liu et al., 2016; Matsui and Mahowald, 2017;

555 Tegen et al., 2019; the value derived from CMIP5 data).

556 Sources of BC and OC are mainly from anthropogenic emissions. Based on the CMIP6
557 data, there are, on average, 7.22 Tg $yr^{-1}$ BC and 13.91 Tg $yr^{-1}$ OC from fossil and bio-fuel
558 emissions and 18.38 Tg $yr^{-1}$ OC from natural emission during the period of 1991 to 2000.
559 Most of them are scavenged through convective and large-scale rainfall processes. The rest
560 returns to the surface by dry deposition. The simulated global BC and OC burdens are 0.13
561 and 0.62 Tg, respectively (Table 6), all close to values of 0.114 Tg BC and 0.69 Tg OC
562 derived from the CMIP5 data, and within the range of 0.11-0.26 Tg BC (Textor et al., 2006;
563 Matsui and Mahowald, 2017; Tegen et al., 2019) and less than the values of 1.25-2.2 Tg OC
564 in other literatures (Textor et al., 2006; Tegen et al., 2019). The simulated BC and OC
565 lifetimes are 6.6 and 5.0 days respectively, and are close to the recent values of 5.0-7.5 days
566 BC and 5.4-6.6 days OC in literatures (Matsui and Mahowald, 2017; Tegen et al., 2019).

567 The emissions of dust and sea salt are mainly determined by winds near the surface. The
568 annual total dust emission in BCC-ESM1 is 2592 Tg $yr^{-1}$, higher than AeroCom multi-model
569 mean (1840 Tg $yr^{-1}$, Textor et al., 2006), but comparable to other studies (Chin et al., 2002;
570 Liu et al., 2012; Matsui and Mahowald, 2017). The average dust loading is 22.93 Tg, lower
571 than the value of 35.9 Tg in Ginoux et al. (2001) but slightly higher than the value of 20.41
572 Tg derived from CMIP5 data. The average lifetime for dust particles is 3.23 days that is
573 shorter than the AeroCom mean (4.14 days) and the value of 3.9 days in recent study (Matsui
574 and Mahowald, 2017). The simulated sea salt emission is 4667.2 Tg $yr^{-1}$, slightly lower than
575 the simulated value in Liu et al. (2012), and substantially lower than the AeroCom mean
576 (16600 Tg $yr^{-1}$, Textor et al., 2006). The simulated sea salt burdens are 11.89 Tg and close to
577 the CMIP5 data. Their averaged lifetimes are 0.93 days and close to the value in the recent of
578 Matsui and Mahowald (2017) but longer than the AeroCom mean (0.41days, Textor et al.,
579 2006).

580 **4.3 Global aerosol distributions at present day**

581 Figures 8-12 show December-January-February (DJF) and June-July-August (JJA) mean
582 column mass concentrations of sulfate ($SO_4^{2-}$), OC, BC, Dust, and Sea Salt aerosols averaged
583 for the period of 1991-2000, respectively. Here, BCC-ESM1 simulated results are compared
584 with the CMIP5-recommended data for the same period. Unlike the pre-industrial level of

585 sulfate shown in Fig. 2, sulfate concentrations at present day (Fig. 8) are strongly influenced
586 by anthropogenic emissions, and have maximum concentrations in the industrial regions (e.g.,
587 East Asia, Europe, and North America). Their seasonal variations are distinct and are
588 characterized by high concentrations in boreal summer and low concentrations in boreal
589 winter. These spatial distributions simulated by BCC-ESM1 are well consistent with the
590 CMIP5 data, with spatial correlation coefficients in DJF and JJA reaching 0.92 and 0.83
591 (Figure 13), respectively. The deviation of the spatial pattern in BCC-ESM1 is less from the
592 CMIP5 data in DJF but larger in JJA (Figure 13).

593 Unlike sulfate whose maximum concentrations are mainly distributed between 60 °N
594 and the equator, peaking concentrations of BC and OC as shown in Figs. 9 and 10 are located
595 near the tropics in the biomass burning regions (e.g., the maritime continent, Central Africa,
596 South America), and their seasonal variations from DJF to JJA are evidently weaker than
597 those of sulfate except in South America. In boreal summer, there are centers of high values
598 in the industrial regions in the Northern Hemisphere mid-latitudes (i.e., East Asia, South Asia,
599 Europe, and North America). These main features of spatial and seasonal variations in CMIP5
600 data are well captured by BCC-ESM1, and the BCC-ESM1 vs. CMIP5 spatial correlation
601 coefficients (Figure 13) are 0.90 (OC in DJF), 0.91 (BC in DJF), 0.91 (OC in JJA) and 0.92
602 (BC in JJA). There are less deviations of spatial pattern for OC in DJF and JJA, but larger
603 deviation for BC from CMIP5 data (Figure 13).

604 As show in Figure 11, dust concentrations in the atmosphere show largest values over
605 strong source regions such as Northern Africa, Southwest and Central Asia, and Australia,
606 and over their outflow regions such as the Atlantic and the western Pacific. In DJF, the
607 CMIP5 data shows centers of high concentrations over East Asia and Central North America,
608 but both centers are missing in BCC-ESM1. However, these two high-value centers in the
609 CMIP5 data may not be true, since frozen soils in these areas in winter lead to unfavorable
610 conditions for soil erosion by winds. The spatial correlation coefficients between CMIP5 and
611 BCC-ESM1 remain high: 0.95 in JJA and 0.88 in DJF (Figure 13). Small deviations of spatial
612 pattern for dust simulations in BCC-ESM1 show less magnitude of dust maximums against
613 with CMIP5 data (Figure 13).

614 As shown in Figure 12, high sea salt concentrations are generally over the storm track

615 regions over the oceans, e.g., mid-latitudes in the Northern Oceans in DJF and the Southern
616 Ocean in JJA where wind speeds and thus sea salt emissions are higher. In addition, there is a
617 belt of high sea salt concentrations in the subtropics of both hemispheres where precipitation
618 scavenging is weak. Their spatial distributions in BCC-ESM1 are consistent with the CMIP5
619 data with correlation coefficients of 0.92 in JJA and 0.90 in DJF (Figure 13). The spatial
620 deviations of sea salt are much closer to CMIP5 data than those of sulfate, OC, BC, and dust
621 distributions (Figure 13).

622 Figure 14 shows vertical distributions of zonally-averaged annual mean concentrations
623 of sulfate, organic carbon, black carbon, dust, and sea salt aerosols in the period of 1991-2000.
624 Both BCC-ESM1 and CMIP5 results show that strong sulfur, OC, and BC emissions in the
625 industrial regions of the Northern Hemisphere mid-latitudes can rise upward and be
626 transported towards the North Pole in the mid- to upper troposphere. Most of OC, BC, and
627 dust aerosols are confined below 500 hPa, while sulfate can be transported to higher altitudes.
628 Sea salt aerosols are mostly confined below 700 hPa, as the particles are large in size and
629 favorable for wet removal and gravitational settling towards the surface. It can be seen that
630 BCC-ESM1 tends to simulate less upward transport of aerosols than the CMIP5 data, likely
631 reflecting the omission of deep convection transport of tracers in BCC-ESM1.

632 The CMIP5 data used here are mainly from model simulations. We will further evaluate
633 the BCC-ESM1 model results with ground observations. Annual mean $SO_4^{2-}$, BC and OC
634 aerosol observations from the Interagency Monitoring of Protected Visual Environments
635 (IMPROVE) sites over 1990-2005 in the United States
636 (http://vista.cira.colostate.edu/IMPROVE/) and from the European Monitoring and Evaluation
637 Programme (EMEP) (http://www.emep.int) sites over 1995-2005 are used. As shown in
638 Figure 15a and 15b, the BCC-ESM simulated sulfate concentrations are in general
639 comparable to the EMEP observations in Europe, but are systematically by about 1 μg $m^{-3}$
640 higher than the U.S. IMPROVE observations. As for BC, there are large model biases at both
641 European and U.S. sites (Figs. 15c and 15d), especially BCC-ESM overestimates BC
642 concentrations at the IMPROVE sites. The observed OC concentrations are slightly
643 overestimated for IMPROVE sites but systematically underestimated for EMEP sites. Some
644 statistical features for simulated concentrations versus EMEP and IMPROVE observations are

listed in Table 7. These comparisons are overall fairly reasonable considering the uncertainties in emissions and the coarse model resolution.

We then evaluate the simulated BC concentrations from BCC-ESM1 with the HIAPER (High-Performance Instrumented Airborne Platform for Environmental Research) Pole-to-Pole Observations (HIPPO) (Wofsy et al., 2011). The HIPPO campaign provided observations of black carbon concentration profiles over Pacific Ocean and North America between 2009 and 2011. Following Tilmes et al. (2016), model results here are sampled along the HIPPO flight tracks and then averaged to different latitude and altitude bands for comparison. As shown in Figure 16, BCC-ESM1 and HIPPO aircraft observations shows reasonable agreement in terms of the spatial distributions and seasonal variations of BC levels. BCC-ESM1 generally reproduces the observed hemispheric gradients of BC, i.e. the larger burden in the NH compared to the SH, in consistent with Figures 10 and 14. The mean value of modelled results along the flight track is 11.1 ng/kg, comparable to 8.2 ng/kg of the HIPPO observations. The model shows large overestimations of BC observations over the tropics, which is also found in the CAM4-chem global chemical model (Tilmes et al., 2016).

### 4.4 Aerosol Optical Properties

Aerosol optical depth (AOD) is an indicator of the reduction in incoming solar radiation (at a particular wavelength) due to scattering and absorption of sunlight by aerosols. In this study, we calculate the AOD at 550 nm for all aerosols including sulfate, BC, organic carbon, sea salt and dust as the product of aerosol dry mass concentrations, aerosol water content, and their specific extinction coefficients. The total AOD is calculated by summing the AOD in each model layer for each aerosol species using the assumption that they are externally mixed. The AOD observations retrieved from MODIS and MISR over the period of 1997-2003, and from AERONET over the period of 1998–2005 (http://aeronet.gsfc.nasa.gov) are used to evaluate the averaged AOD at 550 nm in BCC-ESM. Figure 17 shows averages of MISR and MODIS AOD with corresponding averages from BCC-ESM. The BCC-ESM1 simulated AOD generally captures the spatial distribution of MISR and MODIS retrievals. The model overestimates AOD over East China. It also systematically underestimates the MODIS observations in the Southern Hemisphere, but is closer to MISR observations. Figure

18 shows multi-years annual means of BCC-ESM1 simulated AOD values versus observations from AERONET over the period of 1998–2005. The basic pattern of modeled global AOD is similar to that of observations and their spatial correlation reaches 0.56. Large values of AOD are mainly distributed in land continents such as North African, South Asia, East Asia, Europe, and eastern part of North America. Figures 19a-19d present scatter plots of observed versus simulated multi-year monthly mean AOD at those sites of AERONET in Europe, North America, East Asia, and South Asia over the period of 1998-2005, respectively. Model simulated monthly AOD generally agrees with observations within a factor of 2 for most sites. BCC-ESM slightly overestimates the AOD in European and North American sites. In those regions, BCC-ESM also slightly overestimates MODIS and MISR AOD observations (Fig. 17).

## 5. Summary and discussions

This paper presents a primary evaluation of aerosols simulated in version 1 of the Beijing Climate Center Earth System Model (BCC-ESM1) with the implementation of the interactive atmospheric chemistry and aerosol based on the newly developed BCC-CSM2. Global aerosols (including sulfate, organic carbon, black carbon, dust and sea salt) and major greenhouse gases (e.g., $O_3$, $CH_4$, $N_2O$) in the atmosphere can be interactively simulated when anthropogenic emissions are provided to the model. Concentrations of all aerosols in BCC-ESM1 are determined by the processes of advective transport, emission, gas-phase chemical reactions, dry deposition, gravitational settling, and wet scavenging by clouds and precipitation. The nucleation and coagulation of aerosols are ignored in the present version of BCC-ESM1. Effects of aerosols on radiation, cloud, and precipitation are fully included.

We evaluate the performance of BCC-ESM1 in simulating aerosols and their optical properties in the 20th century following CMIP6 historical simulation according to the requirement of the AerChemMIP. It is forced with anthropogenic emissions evolving from 1850 to 2014 but some WMGHGs such as $CH_4$, $N_2O$, $CO_2$, CFC11 and CFC12 are prescribed using CMIP6 prescribed concentrations (to replace prognostic values of $CH_4$ and $N_2O$ from the chemistry scheme). Both direct and indirect effects of aerosols are considered in BCC-ESM1. Initial conditions of the CMIP6 historical simulation are obtained from a 600-year piControl simulation in the absence of anthropogenic emissions, which well captures

the pre-industrial concentrations of $SO_4^{2-}$, organic carbon (OC), black carbon (BC), dust, and sea salt aerosols and are consistent with the CMIP5 recommended concentrations for the year 1850. With the CMIP6 anthropogenic emissions of $SO_2$, OC, and BC from 1850 to 2014 and their natural emissions implemented in BCC-ESM1, the model simulated $SO_4^{2-}$, BC, and OC aerosols in the atmosphere are highly correlated with the CMIP5-recommended data. The long-term trends of CMIP5 aerosols from 1850 to 2000 are also well simulated by BCC-ESM1. Global budgets of aerosols were evaluated through comparisons of BCC-ESM1 results for 1990-2000 with reports in various literatures for sulfate, BC, OC, sea salt, and dust. Their annual total emissions, atmospheric mass loading, and mean lifetimes are all within the range of values reported in relevant literature. Evaluations of the spatial and vertical distributions of BCC-ESM1 simulated present-day $SO_4^{2-}$, OC, BC, Dust, and sea salt aerosol concentrations against the CMIP5 datasets and in-situ measurements of surface networks (IMPROVE in the U.S. and EMEP in Europe), and HIPPO aircraft observations indicate good agreement among them. The BCC-ESM1 simulates weaker upward transport of aerosols from the surface to the middle and upper troposphere (with reference to CMIP5-recommended data), likely reflecting a lack of deep convection transport of chemical species in the present version of BCC-ESM1. The AOD at 550 nm for all aerosols including sulfate, BC, OC, sea salt, and dust aerosols was further compared with the satellite AOD observations retrieved from MODIS and MISR and surface AOD observations from AERONET. The BCC-ESM1 model results are overall in good agreement with these observations within a factor of 2. All these comparisons demonstrate the success of the implementation of interactive aerosol and atmospheric chemistry in BCC-ESM1.

This work has only evaluated the ability of BCC-ESM1 to simulate aerosols. The variations of aerosols especially for sulfate are related to other gaseous tracers such as OH and $NO_3$ (Table 2), which are determined by the MOZART2 gaseous chemical scheme as implemented in BCC-ESM1, and require further evaluation. As limited length of the text, the other optical feature of aerosols such as extinction coefficients, single scattering albedo and asymmetry parameters, and even their feedbacks on radiation and global temperature change will be explored in the other paper. $O_3$ is evaluated in this work. Other GHGs such as $CH_4$ and

$N_2O$ concentrations can be simulated when forced with emissions and their simulations also need to be evaluated in future.

## 6. Code and data availability

The source codes of BCC-ESM1 model are available for use under licence agreement. Readers interested in BCC-ESM1 codes and the model input files required to reproduce the simulations may contact Dr. Tongwen Wu (twwu@cma.gov.cn) for further details. Model output of BCC CMIP6 AerChemMIP simulations described in this paper refer to Zhang et al. (2019) and is distributed through ESGF and freely accessible through the ESGF data portals after registration. Details about ESGF are presented on the CMIP Panel website at http://www.wcrp-climate.org/index.php/wgcm-cmip/about-cmip.

**Author contributions**

Tongwen Wu led the BCC-ESM1 development. All other co-authors have contributions to it. Fang Zhang and Jie Zhang designed the experiments and carried them out. Tongwen Wu, Laurent Li, Lin Zhang, Xiaohong Liu, Aixue Hu, and Jun Wang wrote the final document with contributions from all other authors.

**Acknowledgements**

This work was supported by The National Key Research and Development Program of China (2016YFA0602100). All the figures are created by the NCAR Command Language (Version 6.6.2) [Software].

**References**

Albani, S., Mahowald, N. M., Perry, A. T., Scanza, R. A., Zender, C. S., Heavens, N. G., Maggi, V., Kok, J. F., and Otto-Bliesner, B. L.: Improved dust representation in the Community Atmosphere Model, J. Adv. Model. Earth Syst., 6, 541–570, doi:10.1002/2013MS000279, 2014.

Albrecht, B.: Aerosols, cloud microphysics, and fractional cloudiness, Science, 245, 1227–1230, 1989.

Arora, V., Boer, G., Friedlingstein, P., Eby, M., Jones, C., Christian, J., Bonan, G., Bopp, L.,

763 Brovkin, V., Cadule, P., Hajima, T., Ilyina, T., Lindsay, K., Tjiputra, J., and Wu, T.:
764 Carbon-concentration and carbon-climate feedbacks in CMIP5 Earth system models. J.
765 Climate, 26, 5289–5314, 2013.
766 Austin, J., Butchart, N., and Shine, K. P.: Possibility of an Arctic ozone hole in a
767 doubled-CO2 climate, Nature, 360, 221–225, 1992
768 Barth, M.C., Rasch, P.J., Kiehl, J.T., Benkowitz, C.M., and Schwartz, S.E.: Sulfur chemistry
769 in the National Center for Atmospheric Research Community Climate Model:
770 Description, evaluation, features, and sensitivity to aqueous chemistry. J. Geophys. Res.,
771 105, D1, 1387-1415, 2000.
772 Bey I., Jacob, D. J., Yantosca, R. M., Logan, J. A., Field, B., Fiore, A. M., Li, Q., Liu, H.,
773 Mickley, L. J., and Schultz, M.: Global modeling of tropospheric chemistry with
774 assimilated meteorology: Model description and evaluation, J. Geophys. Res., 106,
775 23,073-23,096, 2001
776 Boucher, O., Lohmann, U.: The sulphate-CCN-cloud albedo effect – a sensitivity study with
777 two general circulation models, Tellus 47B, 281–300, 1995.
778 Brasseur, G. P., Hauglustaine, D. A., Walters, S., Rasch, P. J., Mu ̈ller, J.-F., Granier, C., and
779 Tie, X. X.: MOZART, a global chemical transport model for ozone and related chemical
780 tracers: 1. Model description, J. Geophys. Res., 103, 28,265– 28,289, 1998.
781 Brasseur, G. P., Tie, X. X., Rasch, P. J., and Lef èvre, F.: A three - dimensional simulation of
782 the Antarctic ozone hole: Impact of anthropogenic chlorine on the lower stratosphere and
783 upper troposphere, J. Geophys. Res., 102, 8909–8930, 1997.
784 Cariolle, D., Lasserre-Bigorry, A., and Royer, J.-F.: A general circulation model simulation of
785 the springtime Antarctic ozone decrease and its impact on midlatitudes, J. Geophys. Res.,
786 95, 1883–1898, 1990.
787 Cess, R. D.: Nuclear war: Illustrative effects of atmospheric smoke and dust upon solar
788 radiation, Clim. Change, 7, 237–251, 1985.
789 Chen, C., and Cotton, W. R.: The physics of the marine stratocumulus-capped mixed layer, J.
790 Atmos. Sci., 44 (50), 2951–2977, 1987.
791 Chin, M., Ginoux, P., Kinne, S., Torres, O., Holben, B.N., Duncan, B.N., Martin, R.V., Logan, J.A.,
792 Higurashi, A., Naka-jima, T.: Tropospheric aerosol optical thickness from the GOCART
793 model and comparisons with satellite and Sun photometer measurements. J. Atmos.
794 Sci. 59:461–483, 2002.

795 Chuang, C. C., Penner, J. E., Taylor, K. E., Grossman, A. S., and Walton, J. J.: An assessment
796 of the radiative effects of anthropogenic sulfate, J. Geophys. Res., 102, 3761–3778,
797 1997.
798 Collins, W. J., Lamarque, J.–F., Schulz, M., Boucher, O., Eyring, V., Hegglin, M. I.,
799 Maycock, A., Myhre, G., Prather, M., Shindell, D., Smith, S. J.: AerChemMIP:
800 quantifying the effects of chemistry and aerosols in CMIP6, Geosci. Model Dev., 10,
801 585–607, 2017.
802 Collins, W. D., Rasch, P. J., Boville, B. A., Hack, J. J., McCaa, J. R., Williamson, D. L,.
803 Kiehl, J. T., Briegleb, B. P., Bitz, C., Lin, S.-J., Zhang, M., and Dai, Y.: Description of
804 the NCAR Community Atmosphere Model (CAM3). Nat. Cent. for Atmos. Res.,
805 Boulder, Colo., 2004.
806 Cooke, W.F., Wilson, J.J.N.: A global black carbon aerosol model. J. Geophys. Res. Atmos.
807 101, 19395–19409, 1996.
808 Cunnold, D., Alyea, F., Phillips, N., Prinn, R.: A three-dimensional dynamical-chemical
809 model of atmospheric ozone, J. Atmos. Sci., 32, 170-194, 1975.
810 Dentener, F., Kinne, S., Bond, T., Boucher, O., Cofala, J., Generoso, S., Ginoux, P., Gong, S.,
811 Hoelzemann, J. J., Ito, A., Marelli, L., Penner, J. E., Putaud, J.-P., Textor, C., Schulz, M.,
812 van der Werf, G. R., and Wilson, J.: Emissions of primary aerosol and precursor gases in
813 the years 2000 and 1750 prescribed data-sets for AeroCom, Atmos. Chem. Phys., 6,
814 4321–4344, doi:10.5194/acp-6-4321-2006, 2006.
815 Eyring, V., Bony, S., Meehl, G. A., Senior, C. A., Stevens, B., Stouffer, R. J., and Taylor, K.
816 E.: Overview of the Coupled Model Intercomparison Project Phase 6 (CMIP6)
817 experimental design and organization, Geosci. Model Dev., 9, 1937–1958,
818 doi:10.5194/gmd-9-1937-2016, 2016.
819 Feichter, J., Kjellstrom, E., Rodhe, H., Dentener, F., Lelieveldi, J., Roelofs, G.-J.: Simulation
820 of the tropospheric sulfur cycle in a global climate model, 30: 1693-1707, 1996.
821 Feng, L., Smith, S. J., Braun, C., Crippa, M., Gidden, M. J., Hoesly, R., Klimont, Z., van
822 Marle, M., van den Berg, M., and van der Werf, G. R.: Gridded Emissions for CMIP6,
823 Geosci. Model Dev. Discuss., https://doi.org/10.5194/gmd-2019-195, 2019
824 Ghan, S. J. and Easter, R. C.: Impact of cloud-borne aerosol representation on aerosol direct
825 and indirect effects, Atmos. Chem. Phys., 6, 4163–4174, 2006.
826 Ginoux, P., M. Chin, I. Tegen, J. M. Prospero, B. Holben, O. Dubovik, and S.-J. Lin (2001),

827 Sources and distributions of dust aerosols simulated with the GOCART model, J.
828 Geophys. Res., 106, 20,255 – 20,274.
829 Giorgi, F., and Chameides, W. L.: The rainout parameterization in a photochemical model, J.
830 Geophys. Res., 90, 7872–7880, 1985.
831 Guenther, A. B., Jiang, X., Heald, C. L., et al.: The Model of Emissions of Gases and
832 Aerosols from Nature Version 2.1 (MEGAN2.1): An Extended and Updated Framework
833 for Modeling Biogenic Emissions. Geoscientific Model Development 5(6): 1471–1492,
834 2012.
835 Guenther, A., Baugh, B. Brasseur, G., Greenberg, J., Harley, P., Klinger, L,. Serca, D., and
836 Vierling, L.: Isoprene emission estimates and uncertainties for the Central African
837 EXPRESSO study domain, J. Geophys. Res., 104(D23), 30, 625–630, 639, 1999.
838 Hess, M., Koepke, P., Schult, I.: Optical properties of aerosols and clouds: the software
839 package OPAC, Bull. Am. Meteorol. Soc., 79, 831–844, 1998.
840 Hoesly, R. M., Smith, S. ., Feng, L., Klimont, Z., Janssens-Maenhout, G., Pitkanen, T.,
841 Seibert, J. J., Vu, L., Andres, R. J., Bolt, R. M., Bond, T. C., Dawidowski, L., Kholod, N.,
842 Kurokawa, J., Li, M., Liu, L., Lu, Z., Moura, M. C. P., O'Rourke, R. R., and Zhang Q.:
843 Historical (1750–2014) anthropogenic emissions of reactive gases and aerosols from the
844 Community Emission Data System (CEDS), Geosci. Model Dev., 11, 369-408, 2018
845 Horowitz, L.W., Walters, S., Mauzerall, D. L., Emmons, L. K., Rasch, P. J., Granier, C., Tie,
846 X., Lamarque, J.-F., Schultz, M. G., Tyndall, G. S., Orlando, J. J., Brasseur, G. P.: A
847 global simulation of tropospheric ozone and related tracers: Description and evaluation
848 of MOZART, version 2, J. Geophys. Res., 108(D24), 4784, doi:10.1029/2002JD002853,
849 2003.
850 Horowitz, L. W.: Past, present, and future concentrations of tropospheric ozone and aerosols:
851 Methodology, ozone evaluation, and sensitivity to aerosol wet removal, J. Geophys. Res.,
852 111, D22211, doi:10.1029/2005JD006937, 2006.
853 Hoffman, F. M., Randerson, J. T., Arora, V. K., Bao, Q., Cadule, P., Ji, D., Jones, C. D.,
854 Kawamiya, M., Khatiwala, S., Lindsay, K., Obata, A., Shevliakova, E., Six, K. D.,
855 Tjiputra, J. F., Volodin, E. M., and Wu, T.: Causes and implications of persistent
856 atmospheric carbon dioxide biases in Earth System Models, J. Geophys. Res. Biogeosci.,
857 119, 141–162, doi:10.1002/2013JG002381, 2014.
858 Holtslag, A. A. M., and Boville, B. A.: Local versus nonlocal boundary-layer diffusion in a

859 global climate model, J. Climate, 6, 1825–1842, 1993.
860 Hurtt, G.C., Chini, L.P., Frolking, S. et al.: Harmonization of land-use scenarios for the period
861 1500–2100: 600 years of global gridded annual land-use transitions, wood harvest, and
862 resulting secondary lands, Climatic Change, 109, 117-161, 2011.
863 Hurtt, G., et al.: input4MIPs.UofMD.landState.CMIP.UofMD-landState-2-1-h, version
864 20170126, Earth Syst. Grid Fed., http://doi.org/10.22033/ESGF/input4MIPs.1127, 2017.
865 Jacobson, M.Z.: Investigating cloud absorption effects: global absorption properties of black
866 carbon, tar balls, and soil dust in clouds and aerosols. J. Geophys. Res. 117, D06205,
867 2012.
868 Jones, C.D., Arora, V., Friedlingstein, P., Bopp, L., Brovkin, V., Dunne, J., Graven, H.,
869 Hoffman, F., Ilyina, T., John, J. G., Jung, M., Kawamiya, M., Koven, C., Pongratz, J.,
870 Raddatz, T., Randerson, J. T., and Zaehle, S.: C4MIP – The Coupled Climate–Carbon
871 Cycle Model Intercomparison Project: experimental protocol for CMIP6, Geosci. Model
872 Dev., 9, 2853–2880, doi:10.5194/gmd-9-2853-2016, 2016.
873 Lamarque, J.-F., Shindell, D. T., Josse, B., Young, P. J., Cionni, I., Eyring, V., Bergmann, D.,
874 Cameron-Smith, P., Collins,W. J., Doherty, R., Dalsoren, S., Faluvegi, G., Folberth, G.,
875 Ghan, S. J., Horowitz, L. W., Lee, Y. H., MacKenzie, I. A., Nagashima, T., Naik, V.,
876 Plummer, D., Righi, M., Rumbold, S. T., Schulz, M., Skeie, R. B., Stevenson, D. S.,
877 Strode, S., Sudo, K., Szopa, S.,Voulgarakis, A., and Zeng, G.: The Atmospheric
878 Chemistry and Climate Model Intercomparison Project (ACCMIP): overview and
879 description of models, simulations and climate diagnostics, Geosci. Model Dev., 6, 179–
880 206, doi:10.5194/gmd-6-179-2013, 2013.
881 Lamarque, J.-F., Emmons, L. K., Hess, P. G., Kinnison, D. E., Tilmes, S., Vitt, F., Heald, C.
882 L., Holland, E. A., Lauritzen, P. H., Neu, J., Orlando, J. J., Rasch, P. J., and Tyndall, G.
883 K.: CAM-chem: description and evaluation of interactive atmospheric chemistry in the
884 Community Earth System Model, Geosci. Model Dev., 5, 369–411, 2012
885 Lamarque, J.-F., Bond, T. C., Eyring, V., Granier, C., Heil, A., Klimont, Z., Lee, D., Liousse,
886 C., Mieville, A., Owen, B., Schultz, M. G., Shindell, D., Smith, S. J., Stehfest, E., Van
887 Aardenne, J., Cooper, O. R., Kainuma, M., Mahowald, N., McConnell, J. R., Naik, V.,
888 Riahi, K., and van Vuuren, D. P.: Historical (1850–2000) gridded anthropogenic and
889 biomass burning emissions of reactive gases and aerosols: methodology and application,
890 Atmos. Chem. Phys., 10, 7017-7039, https://doi.org/10.5194/acp-10-7017-2010, 2010.

Lawrence, D. M., Hurtt, G. C., Arneth, A., Brovkin, V., Calvin, K. V., Jones, A. D., Jones, C. D., Lawrence, P. J., de Noblet-Ducoudré, N., Pongratz, J., Seneviratne, S. I., and Shevliakova, E.: The Land Use Model Intercomparison Project (LUMIP) contribution to CMIP6: rationale and experimental design, Geosci. Model Dev., 9, 2973–2998, https://doi.org/10.5194/gmd-9-2973-2016, 2016.

Lohmann, U., Feichter, J., Penner, J. E., and Leaitch, W. R.: Indirect effect of sulfate and carbonaceous aerosols: A mechanistic treatment. J. Geophys. Res, 105, 12193–12206, 2000

Li, W., Zhang, Y., Shi, X., Zhou, W., Huang, A., Mu, M., Qiu, B., JI, J.: Development of the Land Surface Model BCC_AVIM2.0 and Its Preliminary Performance in LS3MIP/CMIP6, J. Meteor. Res., 33, 851-869, doi: 10.1007/s13351-019-9016-y, 2019.

Liu, X. H., Penner, J. E., and Herzog, M.: Global modeling of aerosol dynamics: Model description, evaluation, and interactions between sulfate and nonsulfate aerosols, J. Geophys. Res.-Atmos., 110, D18206, doi:10.1029/2004jd005674, 2005.

Liu, X., Easter, R.C. Ghan, S.J., Zaveri, R., Rasch, P., Shi, X., Lamarque, J.-F., Gettelman, A., Morrison, H., Vitt, F., Conley, A., Park, S., Neale, R., Hannay, C., Ekman, A.M., Hess, P., Mahowald, N., Collins, W., Iacono, M.J., Bretherton, C.S., Flanner, M.G., and Mitchell, D.: Toward a Minimal Representation of Aerosols in Climate Models: Description and Evaluation in the Community Atmosphere Model CAM5. Geos.Model.Dev. 5(3):709-739. 2012.

Liu, X., Ma, P. -L., Wang, H., Tilmes, S., Singh, B., Easter, R. C., Ghan, S. J., and Rasch, P. J.: Description and evaluation of a new four-mode version of the Modal Aerosol Module (MAM4) within version 5.3 of the Community Atmosphere Model, Geosci. Model Dev., 9, 505–522, https://doi.org/10.5194/gmd-9-505-2016, 2016.

Liu, J., Mauzerall, D.L., Horowitz, L.W., Ginoux, P., Fiore, A.M.: Evaluation intercontinental transport of fine aerosols: (1) methodology, global aerosol distribution and optical depth. Atmos Environ 43:4327–4338, 2009.

Lu, X., Zhang, L., Wu, T., Long, M., Wang, J., Jacob, D., Zhang F., Zhang, J., Eastham, S., Hu, L., Zhu, L., Liu, X., an Wei, M.: Development of the global atmospheric general circulation-chemistry model BCC-GEOS-Chem v1.0: model description and evaluation, submitted to Geos.Model.Dev.

Mahowald, N., Lamarque, J.-F., Tie, X., and Wolff, E.: Sea salt aerosol response to climate

change: last glacial maximum, preindustrial and doubled carbon dioxide climates, J. Geophys. Res., 111, D05303, doi:10.1029/2005JD006459, 2006.

Martin, R. V., et al.: Interpretation of TOMS observations of tropical tropospheric ozone with a global model and in situ observations, J. Geophys. Res., 107(D18), 4351, doi:10.1029/2001JD001480, 2002.

Matsui, H., and Mahowald, N.: Development of a global aerosol model using a two-dimensional sectional method: 2. Evaluation and sensitivity simulations, J. Adv. Model. Earth Syst., 9, 1887–1920, doi:10.1002/2017MS000937, 2017.

Matthes, K., Funke, B., Andersson, M. E., Barnard, L., Beer, J., Charbonneau, P., Clilverd, M. A., Dudok de Wit, T., Haberreiter, M., Hendry, A., Jackman, C. H., Kretzschmar, M., Kruschke, T., Kunze, M., Langematz, U., Marsh, D. R., Maycock, A. C., Misios, S., Rodger, C. J., Scaife, A. A., Seppälä, A., Shangguan, M., Sinnhuber, M., Tourpali, K., Usoskin, I., van de Kamp, M., Verronen, P. T., and Versick, S.: Solar forcing for CMIP6 (v3.2), Geosci. Model Dev., 10, 2247–2302, https://doi.org/10.5194/gmd-10-2247-2017, 2017.

Meinshausen, M., Vogel, E., Nauels, A., Lorbacher, K., Meinshausen, N., Etheridge, D. M., Fraser, P. J., Montzka, S. A., Rayner, P. J., Trudinger, C. M., Krummel, P. B., Beyerle, U., Canadell, J. G., Daniel, J. S., Enting, I. G., Law, R. M., Lunder, C. R., O'Doherty, S., Prinn, R. G., Reimann, S., Rubino, M., Velders, G. J. M., Vollmer, M. K., Wang, R. H. J., and Weiss, R.: Historical greenhouse gas concentrations for climate modelling (CMIP6), Geosci. Model Dev., 10, 2057–2116, https://doi.org/10.5194/gmd-10-2057-2017, 2017.

Mora, C., Wei, C.-L., Rollo, A., Amaro, T., Baco, A.R., Billett, D., Bopp, L., Chen, Q., Collier, M., Danovaro, R., Gooday, A.J., Grupe, B.M., Halloran, P.R., Ingels, J., Jones, D.O.B., Levin, L.A., Nakano, H., Norling, K., Ramirez-Llodra, E., Rex, M., Ruh, H.A., Smith, C.R., Sweetman, A.K., Thurber, A.R., Tjiputra, J. F., Usseglio, P., Watling, L., Wu, T., Yasuhara, M.: Biotic and human vulnerability to projected ocean biogeochemistry change over the 21st century, PLoS Biol 11(10): e1001682. doi:10.1371/journal.pbio.1001682, 2013.

NCAR Command Language (Version 6.6.2) [Software], Boulder, Colorado: UCAR/NCAR/CISL/TDD. http://dx.doi.org/10.5065/D6WD3XH5, 2019.

Neale, R. B., et al.: Description of the NCAR Community Atmosphere Model (CAM 4.0), NCAR Tech. Note, TN-485, pp. 212, Natl. Cent. for Atmos. Res., Boulder, Colo., 2010

955 Neu, J. L. and Prather, M. J.: Toward a more physical representation of precipitation
956 scavenging in global chemistry models: cloud overlap and ice physics and their impact
957 on tropospheric ozone, Atmos. Chem. Phys. Discuss., 11, 24413–24466,
958 doi:10.5194/acpd-11-24413-2011, 2011.
959 Olivier, J.G.J., Bouwman, A.F., Van der Maas, C.W.M., Berdowski, J.J.M., Veldt, C., Bloos,
960 J.P.J., Visschedijk, A.J.H., Zandveld, P.Y.J., Haverslag, J.L., Description of EDGAR
961 Version 2.0: A set of global emission inventories of greenhouse gases and ozone
962 depleting substances for all anthropogenic and most natural sources on a per country
963 basis and on 1° x1° grid. RIVM Techn. Report nr. 771060002, TNO-MEP report nr.
964 R96/119.Nat. Inst. Of Public Health and the Environment/ Netherlands Organisation for
965 Applied Scientific Research, Bilthoven, 1996.
966 Peng, Y., and Lohmann, U.: Sensitivity study of the spectral dispersion of the cloud droplet
967 size distribution on the indirect aerosol effect, Geophys. Res. Lett., 30(10), 1507,
968 doi:10.1029/2003GL017192, 2003.
969 Price, C., and Rind, D.: A simple lightning parameterization for calculating global lightning
970 distributions, J. Geophys. Res., 97, 9919-9933, 1992.
971 Quaas, J., Boucher, O., and Lohmann, U.: Constraining the total aerosol indirect effect in
972 the LMDZ and ECHAM4 GCMs using MODIS satellite data. Atmos Chem Phys 6,947–
973 955, 2006.
974 Sander, S., Friedl, R. R., Ravishankara, A. R., et al.: Chemical Kinetics and Photochemical
975 Data for Use in Atmospheric Studies, Evaluation Number 14, JPL Publication 02-25,
976 NASA, Jet Propulsion Laboratory, California Institute of Technology, Pasadena, CA,
977 2003.
978 Schlesinger, M. E., Mintz, Y.: Numerical simulation of ozone production, transport and
979 distribution with a global atmospheric general circulation model, J.Atmos.Sci., 36:
980 1325-1361, 1979.
981 Shindell, D.T., Horowitz, L.W., Schwarzkopf, M.D.: Composition Models in Climate
982 Projections Based on Emissions Scenarios for Long-Lived and Short-Lived Radiatively
983 Active Gases and Aerosols. H.Levy II, D.T. Shindell, A.Gilliland, M.D.Schwarzkopf,
984 L.W.Horowitz, (eds.) .A Report by the U.S.Climate Change Science Program and the
985 Subcommittee on Global Change Research, Washington, D.C., 2008

Solomon, S.: Stratospheric ozone depletion: A review of concepts and history, Reviews of Geophysics, 37, 275–316, 1999.

Taylor, K.E., Stouffer, R. J., Meehl, G. A.: An overview of CMIP5 and the experiment design, Bull. Am. Meteorol. Soc. 93, 485-498, 2012.

Tegen, I., Neubauer, D., Ferrachat, S., Siegenthaler-Le Drian, C., Bey, I., Schutgens, N., Stier, P., Watson-Parris, D., Stanelle, T., Schmidt, H., Rast, S., Kokkola, H., Schultz, M., Schroeder, S., Daskalakis, N., Barthel, S., Heinold, B., and Lohmann, U.: The global aerosol–climate model ECHAM6.3–HAM2.3 – Part 1: Aerosol evaluation, Geosci. Model Dev., 12, 1643–1677, https://doi.org/10.5194/gmd-12-1643-2019, 2019.

Textor, C., Schulz, M., Guibert, S., Kinne, S., Balkanski, Y., Bauer, S., Berntsen, T., Berglen, T., Boucher, O., Chin, M., Dentener, F., Diehl, T., Easter, R., Feichter, H., Fillmore, D., Ghan, S., Ginoux, P., Gong, S., Grini, A., Hendricks, J., Horowitz, L., Huang, P., Isaksen, I., Iversen, I., Kloster, S., Koch, D., Kirkevåg, A., Kristjansson, J. E., Krol, M., Lauer, A., Lamarque, J. F., Liu, X., Montanaro, V., Myhre, G., Penner, J., Pitari, G., Reddy, S., Seland, Ø., Stier, P., Takemura, T., and Tie, X.: Analysis and quantification of the diversities of aerosol life cycles within AeroCom, Atmos. Chem. Phys., 6, 1777–1813, https://doi.org/10.5194/acp-6-1777-2006, 2006.

Thomason, L. W., Ernest, N., Millán, L., Rieger, L., Bourassa, A., Vernier, J. P., Manney, G., Luo, B.P., Arfeuille, F., Peter, T.: A global space‐based stratospheric aerosol climatology: 1979-2016. Earth System Science Data, 10(1), 469–492, doi: 10.5194/essd-10-469-2018, 2018.

Tie, X., Brasseur, G., Emmons, L., Horowitz, L., and Kinnison, D.: Effects of aerosols on tropospheric oxidants: A global model study, J. Geophys. Res., 106, 2931– 2964, 2001.

Tie, X., Madronich, S., Walters, S., Edwards, D., Ginoux, P., Mahowald, N., Zhang, R., Luo, C., and Brasseur, G.: Assessment of the global impact of aerosols on tropospheric oxidants, J. Geophys. Res., 110, D03204, doi:10.1029/2004JD005359, 2005.

Tilmes, S., Lamarque, J.-F., Emmons, L. K., Kinnison, D. E., Marsh, D., Garcia, R. R., Smith, A. K., Neely, R. R., Conley, A., Vitt, F., Val Martin, M., Tanimoto, H., Simpson, I., Blake, D. R., and Blake, N.: Representation of the Community Earth System Model (CESM1) CAM4-chem within the Chemistry-Climate Model Initiative (CCMI), Geoscientific Model Development, 9, 1853-1890, 2016.

Todd-Brown, K.E.O., Randerson, J.T., Hopkins, F., Arora, V., Hajima, T., Jones, C.,

Shevliakova, E., Tjiputra, J., Volodin, E., Wu, T., Zhang, Q., Allison, S.D.: Changes in soil organic carbon storage predicted by Earth system models during the 21st century, Biogeosciences, 11, 2341-2356, 2014.

Van Marle, M.J.E., S. Kloster, B.I. Magi, J.R. Marlon, A.-L. Daniau, R.D. Field, A. Arneth, M. Forrest, S. Hantson, N.M. Kehrwald, W. Knorr, G. Lasslop, F. Li, S. Mangeon, C. Yue, J.W. Kaiser, and G.R. van der Werf, 2017: Historic global biomass burning emissions for CMIP6 (BB4CMIP) based on merging satellite observations with proxies and fire models (1750-2015). Geosci. Model Dev., 10, 3329-3357, doi:10.5194/gmd-10-3329-2017.

Wang, J., Hoffmann, A. A., Park, R., Jacob, D. J., and Martin, S. T.: Global distribution of solid and aqueous sulfate aerosols: effect of the hysteresis of particle phase transitions, J. Geophys. Res., 113, D11206, Doi:11210.11029/12007JD009367, 2008a.

Wang, J., Jacob, D. J., and Martin, S. T.: Sensitivity of sulfate direct climate forcing to the hysteresis of particle phase transitions, J. Geophys. Res., 113, D11207, doi:11210.11029/12007JD009368, 2008b.

Wesely, M. L.: Parameterization of surface resistance to gaseous dry deposition in regional-scale numerical models, Atmos. Environ., 23, 1293–1304, 1989.

Wild, M., Folini, D., Schar, C., Loeb, N., Dutton, E.G., Konig-Langlo, G.: The global energy balance from a surface perspective, Climate Dynamics, 40: 3107-3134, 2013.

Williamson, D. L., and Rasch, P. J.: Two-dimensional semi-Lagrangian transport with shapepreserving interpolation, Mon. Wea. Rev., 117, 102–129, 1989.

Wofsy, S. C. and the HIPPO team: HIAPER Pole-to-Pole Observations (HIPPO): fine-grained, global-scale measurements of climatically important atmospheric gases and aerosols, Philo T. R. Soc. A, 369, 2073–86, doi:10.1098/rsta.2010.0313, 2011.

Wu, T., Song, L., Li, W., Wang, Z., Zhang, H., Xin, X., Zhang, Y., Zhang, L., Li, J., Wu, F., Liu, Y., Zhang, F., Shi, X., Chu, M., Zhang, J., Fang, Y., Wang, F., Lu, Y., Liu, X., Wei, M., Liu, Q., Zhou, W., Dong, M., Zhao, Q., Ji, J., Li, L., Zhou, M.: An overview of BCC climate system model development and application for climate change studies. J. Meteor. Res., 28(1), 34-56, 2014.

Wu, T., Li, W., Ji, J., Xin, X., Li, L., Wang, Z, Zhang, Y., Li, J., Zhang, F., Wei, M., Shi, X., Wu, F., Zhang, L., Chu, M., Jie, W., Liu, Y., Wang, F., Liu, X., Li, Q., Dong, M., Liang, X., Gao, Y., Zhang, J.: Global carbon budgets simulated by the Beijing climate center

climate system model for the last century. J Geophys Res Atmos, 118, 4326-4347. doi: 10.1002/jgrd.50320, 2013.

Wu, T., Lu, Y., Fang, Y., Xin, X., Li, L., Li, W., Jie, W., Zhang, J., Liu, Y., Zhang, L., Zhang, F., Zhang, Y., Wu, F., Li, J., Chu, M., Wang, Z., Shi, X., Liu, X., Wei, M., Huang, A., Zhang, Y., and Liu, X.: The Beijing Climate Center Climate System Model (BCC-CSM): the main progress from CMIP5 to CMIP6, Geos.Model Dev., 12, 1573-1600, http://doi/.org/10.5194/gmd-12-1573-2019, 2019.

Young, P. J., Archibald, A. T., Bowman, K. W., Lamarque, J. F., Naik, V., Stevenson, D. S., Tilmes, S., Voulgarakis, A., Wild, O., Bergmann, D., Cameron-Smith, P., Cionni, I., Collins, W. J., Dalsøren, S. B., Doherty, R. M., Eyring, V., Faluvegi, G., Horowitz, L. W., Josse, B., Lee, Y. H., MacKenzie, I. A., Nagashima, T., Plummer, D. A., Righi, M., Rumbold, S. T., Skeie, R. B., Shindell, D. T., Strode, S. A., Sudo, K., Szopa, S., and Zeng, G.: Pre-industrial to end 21st century projections of tropospheric ozone from the Atmospheric Chemistry and Climate Model Intercomparison Project (ACCMIP), Atmos. Chem. Phys., 13, 2063-2090, http://doi/.org/10.5194/acp-13-2063-2013, 2013.

Young, P. J., Naik, V., Fiore, A. M., Gaudel, A., Guo, J., Lin, M. Y., Neu, J. L., Parrish, D. D., Rieder, H. E., Schnell, J. L., Tilmes, S., Wild, O., Zhang, L., Ziemke, J. R., Brandt, J., Delcloo, A., Doherty, R. M., Geels, C., Hegglin, M. I., Hu, L., Im, U., Kumar, R., Luhar, A., Murray, L., Plummer, D., Rodriguez, J., Saiz-Lopez, A., Schultz, M. G., Woodhouse, M. T., and Zeng, G.: Tropospheric Ozone Assessment Report: Assessment of global-scale model performance for global and regional ozone distributions, variability, and trends, Elem Sci Anth, 6, 10, http://doi/.org/10.1525/elementa.265, 2018.

Zender, C., Bian, H., and Newman, D.: Mineral Dust Entrainment and Deposition (DEAD) model: Description and 1990s dust climatology, J. Geophys. Res., 108(D14), 4416, doi: 10.1029/2002JD002775, 2003.

Zhang, J., Wu, T., Shi, X., Zhang F., Li, J., Chu, M., Liu, Q., Yan, J., Ma, Q., Wei, M.: BCC BCC-ESM1 model output prepared for CMIP6 AerChemMIP. Version YYYYMMDD[1], Earth System Grid Federation, https://doi.org/10.22033/ESGF/CMIP6.1733, 2019.

Table 1. Chemical species considered in BCC-AGCM3-Chem. Species marked with star (*) denote those added in BCC-ESM1 apart from the 63 species used in MOZART2. In the column of surface emission, interactive surface emissions are considered for sea salt and dust.

| Species | | Dry deposition | Wet deposition | Surface emission | Aircraft emission | Volcanic emission |
|---|---|---|---|---|---|---|
| Gas tracers | $O_3$ | √ | | | | |
| | $N_2O$ | | | √ | | |
| | N | | | | | |
| | NO | √ | | √ | √ | |
| | $NO_2$ | √ | | | | |
| | $NO_3$ | | | | | |
| | $HNO_3$ | √ | √ | | | |
| | $HO_2NO_2$ | √ | √ | | | |
| | $N_2O_5$ | | | | | |
| | $CH_4$ | √ | | √ | √ | |
| | $CH_3O_2$ | | | | | |
| | $CH_3OOH$ | √ | √ | | | |
| | $CH_2O$ | √ | √ | √ | | |
| | CO | √ | | √ | √ | |
| | OH | | | | | |
| | $HO_2$ | | | | | |
| | $H_2O_2$ | √ | √ | | | |
| | $C_3H_6$ | | | √ | | |
| | ISOP | | | √ | | |
| | $PO_2$ | | | | | |
| | $CH_3CHO$ | √ | √ | √ | | |
| | POOH | √ | √ | | | |
| | $CH_3CO_3$ | | | | | |
| | $CH_3COOOH$ | √ | √ | | | |
| | PAN | √ | | | | |
| | ONIT | √ | √ | | | |
| | $C_2H_6$ | | | √ | | |
| | $C_2H_4$ | | | √ | | |
| | $C_4H_{10}$ | | | √ | | |
| | MPAN | √ | | | | |
| | $ISOPO_2$ | | | | | |
| | MVK | | √ | | | |
| | MACR | | √ | | | |
| | $MACRO_2$ | | | | | |
| | MACROOH | √ | √ | | | |
| | $MCO_3$ | | | | | |
| | $C_2H_5O_2$ | | | | | |
| | $C_2H_5OOH$ | √ | √ | | | |
| | $C_{10}H_{16}$ | | | √ | | |

1086 Table 1. Continued.

| Species name | | Dry deposition | Wet deposition | Surface emission | Aircraft emission | Volcanic emission |
|---|---|---|---|---|---|---|
| Gas tracers | $C_3H_8$ | | | √ | | |
| | $C_3H_7O_2$ | | | | | |
| | $C_3H_7OOH$ | √ | √ | | | |
| | $CH_3COCH_3$ | √ | | √ | | |
| | ROOH | | √ | | | |
| | $CH_3OH$ | √ | √ | √ | | |
| | $C_2H_5OH$ | √ | √ | √ | | |
| | GLYALD | √ | √ | | | |
| | HYAC | √ | √ | | | |
| | $EO_2$ | | | | | |
| | EO | | | | | |
| | HYDRALD | √ | √ | | | |
| | $RO_2$ | | | | | |
| | $CH_3COCHO$ | √ | √ | √ | | |
| | Rn-222 | | | | | |
| | Pb-210 | √ | √ | | | |
| | $ISOPNO_3$ | | √ | | | |
| | ONITR | √ | √ | | | |
| | $XO_2$ | | | | | |
| | XOOH | √ | √ | | | |
| | ISOPOOH | √ | √ | | | |
| | $H_2$ | √ | | √ | | |
| | Stratospheric $O_3$ | √ | | | | |
| | Inert $O_3$ | √ | | | | |
| | $SO_2$* | √ | √ | √ | √ | √ |
| | DMS* | | | √ | | |
| | $NH_3$* | | | √ | √ | |
| Aerosols | $SO_4^{2-}$* | √ | √ | | | |
| | OC1* | √ | √ | √ | √ | |
| | OC2* | √ | √ | √ | √ | |
| | BC1* | √ | √ | √ | √ | |
| | BC2* | √ | √ | √ | √ | |
| | SSLT01* | √ | √ | | | |
| | SSLT02* | √ | √ | | | |
| | SSLT03* | √ | √ | | | |
| | SSLT04* | √ | √ | | | |
| | DST01* | √ | √ | | | |
| | DST02* | √ | √ | | | |
| | DST03* | √ | √ | | | |
| | DST04* | √ | √ | | | |

1087

1088

Table 2. Gas-phase chemical reactions for $NH_3$ and bulk aerosols precursors following CAM-Chem (Lamarque et al., 2012). The reaction rates ($s^{-1}$) refer to Tie et al. (2001) and Sander et al. (2003), and Cooke and Wilson (1996). Temperature (T) is expressed in K, air density (M) in molecule $cm^{-3}$, ki and ko in $cm^3$ $molecule^{-1}$ $s^{-1}$.

| Chemical reactions | Rate |
|---|---|
| $NH_3$+ OH → $H_2O$ | 1.70E-12*exp(–710/T) |
| $SO_2$ + OH → $SO_4^{2-}$ | ko/(1.+ko*M/ki)*f**(1./(1.+log10(ko*M/ki)), in which ko=3.0E-31*(300/T)**3.3; ki=1.E-12; f =0.6 |
| DMS + OH → $SO_2$ | 9.60E-12*exp(-234./T) |
| DMS + OH → .5*$SO_2$ + .5*$HO_2$ | 1.7E−42*exp(7810/T)*M*0.21/(1+5.5E−31*exp(7460/T)* M* 0.21) |
| DMS + $NO_3$ → $SO_2$ + $HNO_3$ | 1.90E-13*exp( 520/T) |
| BC1 → BC2 | 7.10E-06 |
| OC1 → OC2 | 7.10E-06 |

Table 3. Size and density parameters of bulk aerosols.

| Aerosols | Species Name | Mean radius (μm) / bin size (μm) | Geometric standard deviation (μm) | Density (g $cm^{-3}$) |
|---|---|---|---|---|
| $SO_4^{2-}$ | Sulfate | 0.05 | 2.03 | 1.77 |
| BC1 | hydrophobic black carbon | 0.02 | 2.00 | 1.0 |
| BC2 | hydrophilic black carbon | 0.02 | 2.00 | 1.0 |
| OC1 | hydrophobic organic carbon | 0.03 | 2.24 | 1.8 |
| OC2 | hydrophilic organic carbon | 0.03 | 2.24 | 1.8 |
| DST01 | Dust | 0.55/ bin: 0.1-1.0 | 2.00 | 2.5 |
| DST02 | Dust | 1.75 / bin: 1.0-2.5 | 2.00 | 2.5 |
| DST03 | Dust | 3.75 / bin: 2.5-5.0 | 2.00 | 2.5 |
| DST04 | Dust | 7.50 / bin: 5.0-10. | 2.00 | 2.5 |
| SSLT01 | Sea salt | 0.52 / bin: 0.2-1.0 | 2.00 | 2.2 |
| SSLT02 | Sea salt | 2.38 / bin: 1.0-3.0 | 2.00 | 2.2 |
| SSLT03 | Sea salt | 4.86 / bin: 3.0-10. | 2.00 | 2.2 |
| SSLT04 | Sea salt | 15.14 / bin: 10.-20. | 2.00 | 2.2 |

Table 4. Source of emission data. MOZART2 data denote the standard tropospheric chemistry package for MOZART contains surface emissions from the EDGAR 2.0 data base (Olivier et al., 1996). ACCMIP data are downloaded from the IPCC ACCMIP emission inventory (http://accent.aero.jussieu.fr/ACCMIP.php) and they vary from 1850 to 2000, in 10-year steps (Lamarque et al., 2010). CMIP6 data are from https://esgf-node.llnl.gov/search/input4mips/. Anthropogenic emission includes Industrial and fossil fuel use, agriculture, ships, and etc. Biomass burning includes vegetation fires incl. fuel wood and agricultural burning.

| Species | Anthropogenic emission | Biomass burning | Biogenic emissions from vegetation | Biogenic emissions from soil | Oceanic emissions | Airplane emission | Volcanic emission |
|---|---|---|---|---|---|---|---|
| $C_2H_4$ | CMIP6 | CMIP6 | On-line computation | | MOZART2 | | |
| $C_2H_5OH$ | CMIP6 | CMIP6 | | | | | |
| $C_2H_6$ | CMIP6 | CMIP6 | ACCMIP | | MOZART2 | | |
| $C_3H_6$ | CMIP6 | CMIP6 | On-line computation | | MOZART2 | | |
| $C_3H_8$ | CMIP6 | CMIP6 | ACCMIP | | MOZART2 | | |
| $C_4H_{10}$ | CMIP6 | CMIP5 | MOZART2 | | MOZART2 | | |
| $CH_2O$ | CMIP6 | CMIP6 | | | | | |
| $CH_3CHO$ | ACCMIP | CMIP6 | | | | | |
| $CH_3COCHO$ | | CMIP6 | | | | | |
| $CH_3OH$ | ACCMIP | CMIP6 | ACCMIP | | | | |
| $CH_3COCH_3$ | ACCMIP | ACCMIP | On-line computation | | MOZART2 | | |
| ISOP | | CMIP5 | On-line computation | | | | |
| $C_{10}H_{16}$ | | CMIP6 | On-line computation | | | | |
| $CH_4$ | CMIP6 | CMIP6 | MOZART2 | | MOZART2 | CMIP6 | |
| CO | CMIP6 | CMIP6 | ACCMIP | MOZART2 | ACCMIP | CMIP6 | |
| $H_2$ | MOZART2 | CMIP6 | | MOZART2 | MOZART2 | | |
| $N_2O$ | MOZART2 | CMIP6 | | MOZART2 | MOZART2 | | |
| $NH_3$ | CMIP6 | CMIP6 | | ACCMIP | ACCMIP | CMIP6 | |
| NO | CMIP6 | CMIP6 | | ACCMIP | | CMIP6 | |
| $SO_2$ | CMIP6 | CMIP6 | | | | CMIP6 | ACCMIP |
| DMS | | | | | ACCMIP | | |
| OC1 | CMIP6 | CMIP6 | | | | CMIP6 | |
| OC2 | CMIP6 | CMIP6 | On-line computation | | | CMIP6 | |
| BC1 | CMIP6 | CMIP6 | | | | CMIP6 | |
| BC2 | CMIP6 | CMIP6 | | | | CMIP6 | |

Table 5. Global budgets for DMS, $SO_2$, and sulfate in the period of 1991 to 2000. Units are sources and sinks, Tg(S) $yr^{-1}$; burden, Tg; lifetime, days.

| | | BCC-ESM (1991-2000 mean) | Other studies and CMIP5 data |
|---|---|---|---|
| DMS | Sources | 27.4 | |
| | Emission | 27.4 | 10.7-23.7[a] |
| | Sinks | 28.0 | |
| | Gas-phase oxidation | 28.0 | |
| | Burden | 0.12 | 0.04-0.29[a] |
| | Lifetime | 0.78 | 0.5-3.0[a] |
| $SO_2$ | Sources | 76.93 | |
| | Emission at surface | 63.63 | |
| | Emission from airplane | 0.10 | |
| | DMS oxidation | 13.20 | 10.0-24.7[a] |
| | Sinks | 76.96 | |
| | Dry deposition | 18.53 | 16.0-55.0[a] |
| | Wet deposition | 9.36 | 0.0-19.9[a] |
| | Gas-phase oxidation | 10.33 | 6.1-16.8[a] |
| | Aqueous-phase oxidation | 38.74 | 24.5-57.8[a] |
| | Burden | 0.48 | 0.40-1.22[a] |
| | Lifetime | 1.12 | 0.6-2.6[a] |
| $SO_4^{2-}$ | Sources | 49.05 | 59.67±13.13[b] |
| | Emission | 0.00 | |
| | $SO_2$ aqueous-phase oxidation | 38.73 | |
| | $SO_2$ gas-phase oxidation | 10.32 | |
| | Sinks | 49.06 | |
| | Dry deposition | 2.20 | 4.96-5.51[d] |
| | Wet deposition | 46.86 | 39.34-40.20[d] |
| | Burden | 1.89 | 1.98±0.48[b], 1.71[c],1.2[g], 2.22-2.43[h] |
| | Lifetime | 4.69 | 4.12±0.74[b], 3.72-3.77[d] 3.3[g], 3.7-4.0[h] |

Notes: References denote a for Liu et al. (2005), b for Textor et al. (2006), c for the values derived from CMIP5 prescribed aerosol masses averaged from 1991 to 2000, d for Liu et al. (2012), g for Matsui and Mahowald (2017), and h for Tegen et al. (2019). Values of DMS, $SO_2$, and sulfate burdens in the literature d are transferred from TgS to Tg (species) for units consistence.

Table 6. Same as Table 5, but for global budgets for black carbon, organic carbon, dust, and sea salts. Units are sources and sinks, Tg $yr^{-1}$; burden, Tg; lifetime, days.

| | | BCC-ESM (1991-2000 mean) | Other studies and CMIP5 data |
|---|---|---|---|
| BC | Sources | 7.22 | |
| | Emission | 7.22 | 11.9±2.7[b], 7.8[g] |
| | Sinks | 7.24 | 7.75[d], 7.8[g] |
| | Dry deposition | 0.90 | 0.27[g], 1.30-1.64[e] |
| | Wet deposition | 6.34 | 7.5[g], 6.10-6.45[e] |
| | Burden | 0.13 | 0.114[c], 0.24±0.1[b], 0.11[g],0.14-0.26[h], 0.084-0.123[e] |
| | Lifetime | 6.60 | 7.12±2.35[b], 3.95-4.80[e], 5.0[g], 6.3-7.5[h] |
| OC | Sources | 32.29 | |
| | Fossil and biofuel emission | 13.91 | |
| | Natural emission | 18.38 | |
| | Sinks | 32.30 | |
| | Dry deposition | 2.44 | |
| | Wet deposition | 29.86 | |
| | Burden | 0.62 | 0.69[c], 1.7±0.45[b],1.0-2.2[h] |
| | Lifetime | 5.00 | 6.54±1.76[b], 4.56−4.90[d], 6.4[g],5.4-6.6[h] |
| Dust | Sources | 2592.0 | 1840[b],2943.5−3121.9[d], 2677[g] |
| | Sinks | 2592.0 | |
| | Dry deposition | 1630.8 | 1444[g] |
| | Wet deposition | 961.2 | 1245[g] |
| | Burden | 22.93 | 20.41[c], 22.424.7[d], 35.9[f], 19.2±7.68[b], 28.5[g], 16.5-17.9[h] |
| | Lifetime | 3.23 | 4.14±1.78[b], 2.61−3.07[d], 3.9[g], 5.3-5.7[h] |
| Sea Salt | Sources | 4667.2 | 4965.5-5004.1[d], 5039[g] |
| | Sinks | 4667.4 | |
| | Dry deposition | 2978.5 | 2158[g] |
| | Wet deposition | 1688.9 | 2918[g] |
| | Burden | 11.89 | 7.58−10.37[a], 6.4±3.4[b], 11.84[c], 13.6[g], 3.9[h] |
| | Lifetime | 0.93 | 0.41±0.24[b],0.55−0.76[d], 0.98[g], 1.2-1.3[h] |

Notes: References denote a for Liu et al. (2005), b for Textor et al. (2006), c derived from CMIP5 prescribed aerosol masses averaged from 1991 to 2000, d for Liu et al. (2012), e for Liu et al. (2016), f for Ginoux (2001), g for Matsui and Mahowald (2017), and h for Tegen et al. (2019).

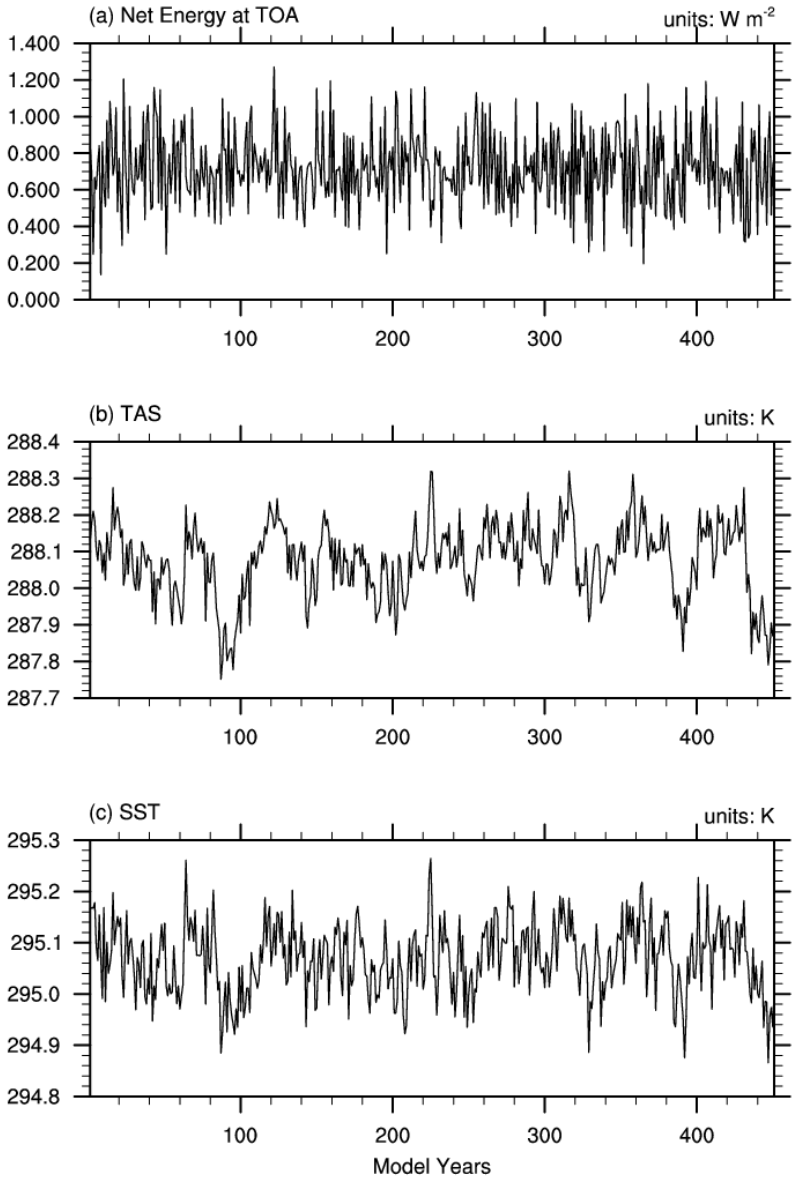


Figure 1. The time series of global and annual mean of (a) net energy budget at top of atmosphere (W m$^{-2}$), (b) near-surface air temperature (K), and (c) sea surface temperature (K) in the last 450 years of the piControl simulation.

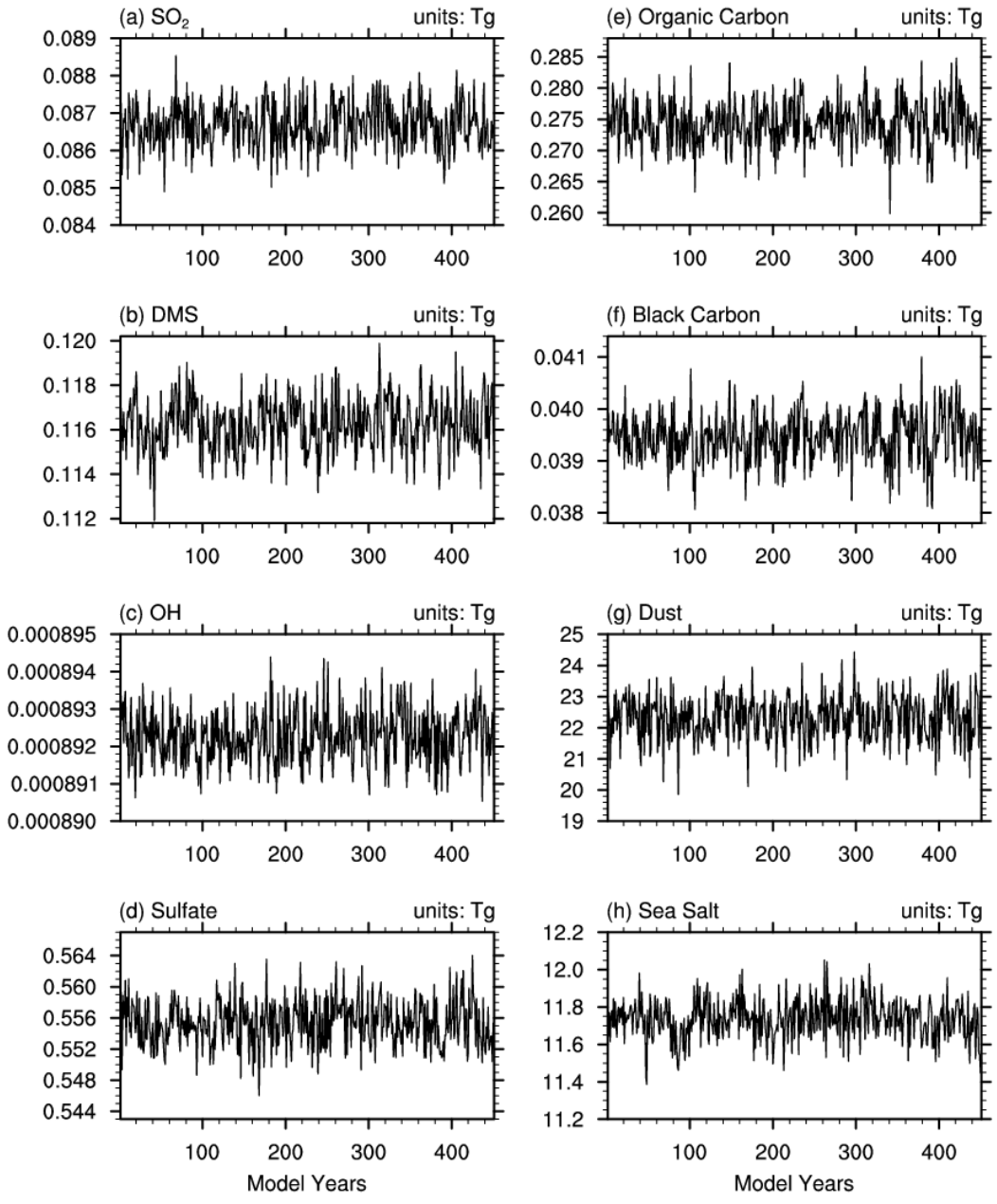


Figure 2. Same as in Figure 1, but for the global burdens of (a) $SO_2$, (b) DMS, (c) OH, and (d-h) different aerosols in the troposphere (below 100 hPa). Units are Tg.

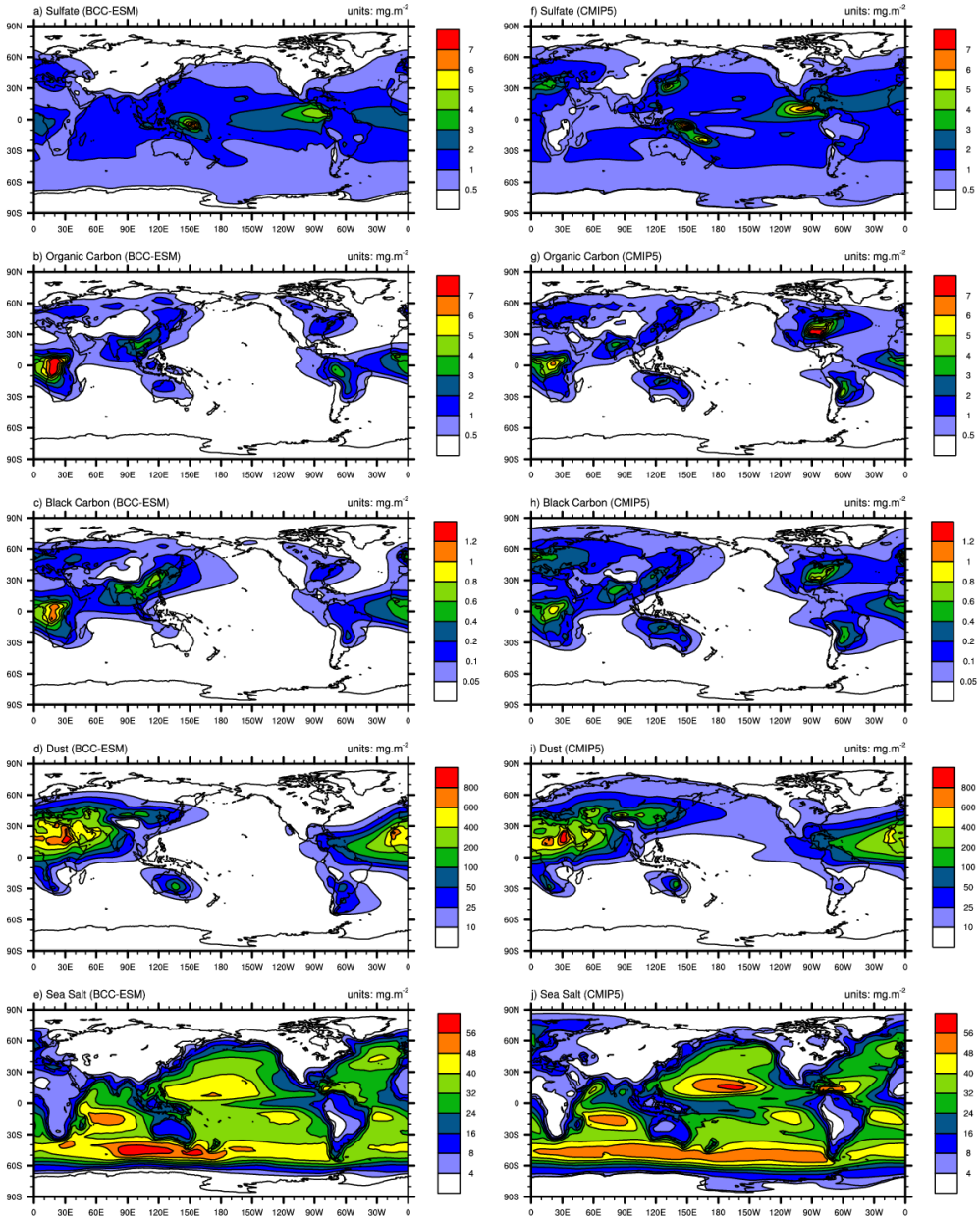


Figure 3. Global distributions of annual mean mass burdens of sulfate ($SO_4^{2-}$; first row), organic carbon (OC; second row), black carbon (BC; third row), dust (fourth row), and sea salt (fifth row) aerosols in the whole atmospheric column. The left panels show the mean averaged for the last 100 years of BCC-ESM pre-industrial piControl simulations, and the right panels show the CMIP5 recommended aerosol concentrations in year 1850 (the website at IIASA http://tntcat.iiasa.ac.at/RcpDb/.). Units: mg $m^{-2}$.

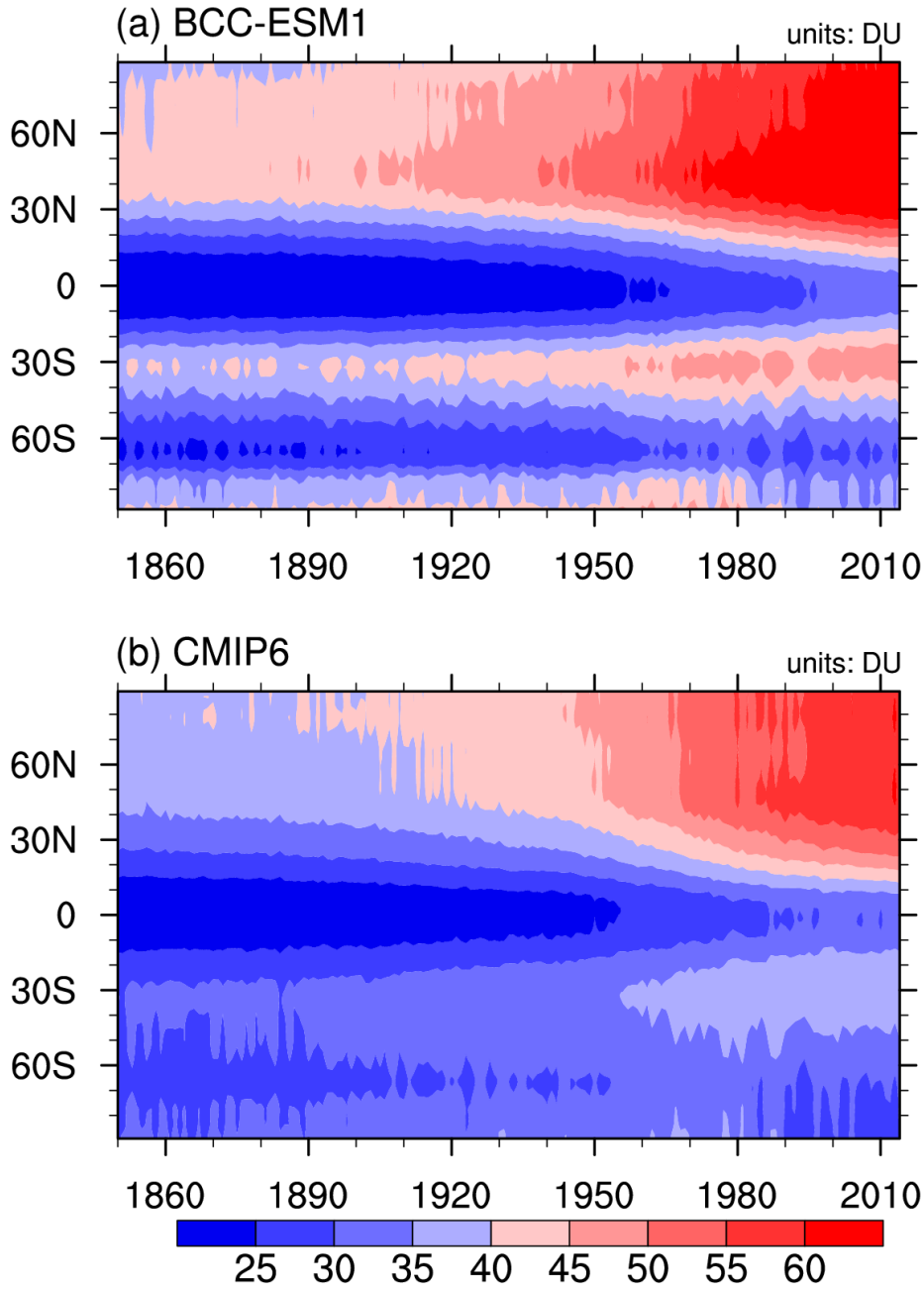


Figure 4. Zonal mean of yearly mean concentration of ozone column in the troposphere below 300 hPa to the ground from 1871 to 1999 for (a) BCC-ESM1 and (b) CMIP6 data. Unit: DU.

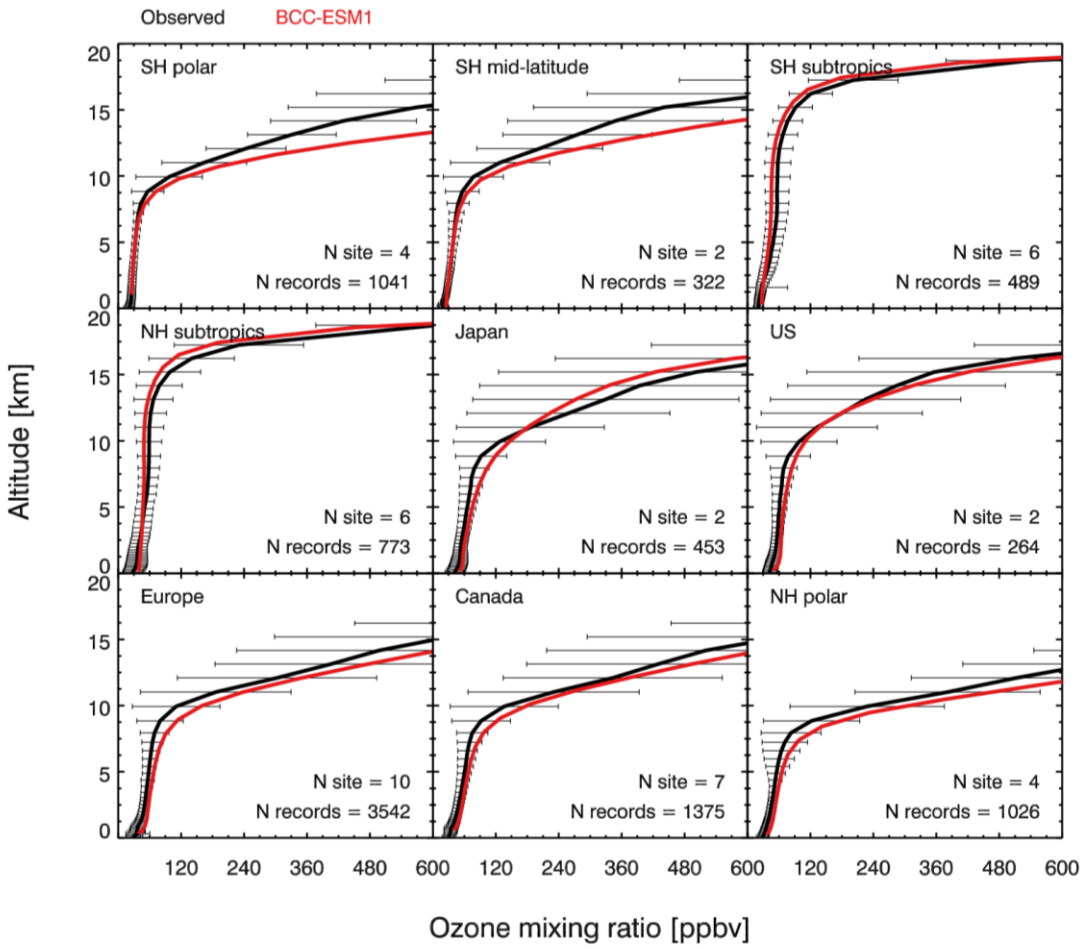


Figure 5. Vertical profiles of annual mean ozone concentrations from observations averaged for 2010-2014 in nine regions (black) and from the BCC-ESM1 simulations (red). The observations are derived from 41 global WOUDC sites.

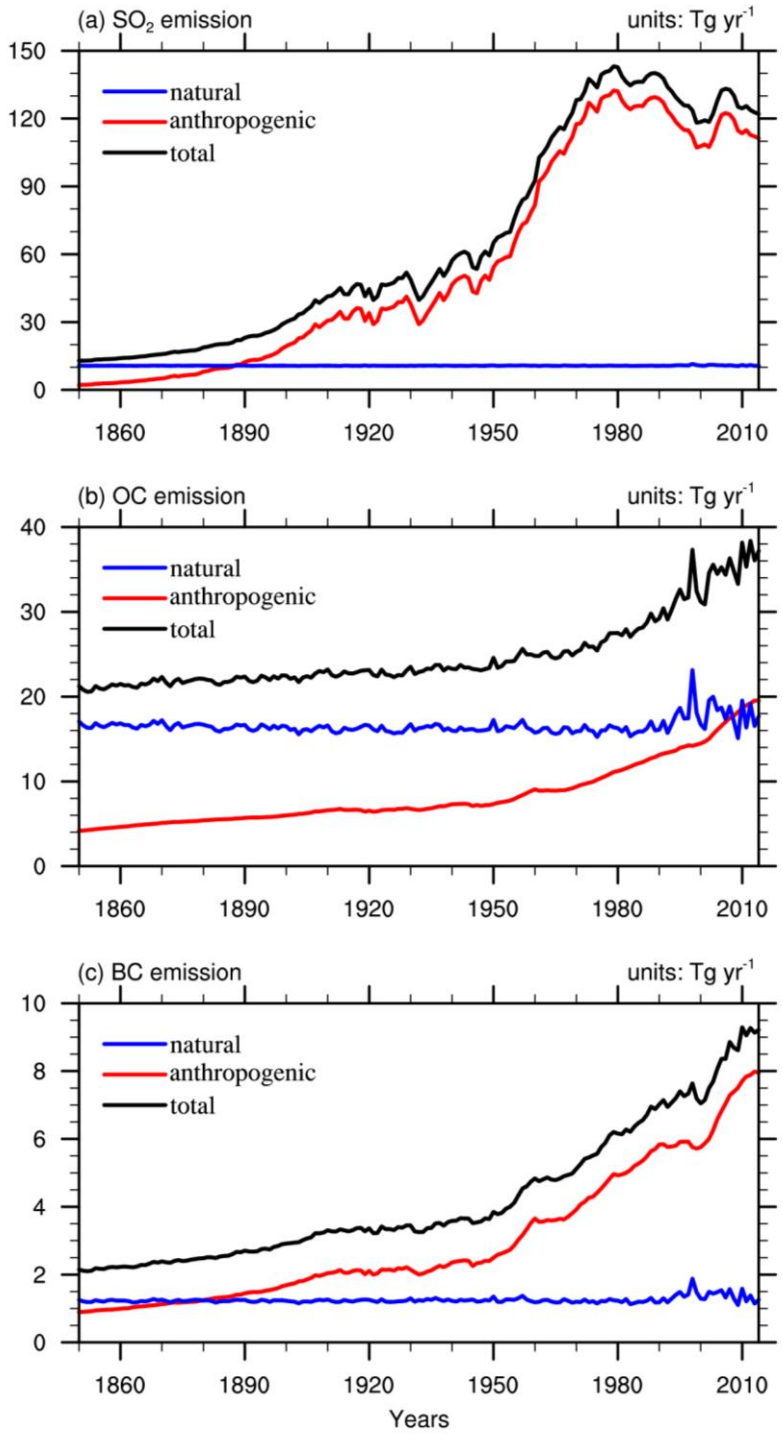


Figure 6. Global annual anthropogenic, natural, and total emissions of $SO_2$, organic carbon (OC), and black carbon (BC) in the BCC-ESM1 historical simulation. All the biomass burning emissions are included in natural emissions in (a)-(c). Units: Tg $yr^{-1}$.

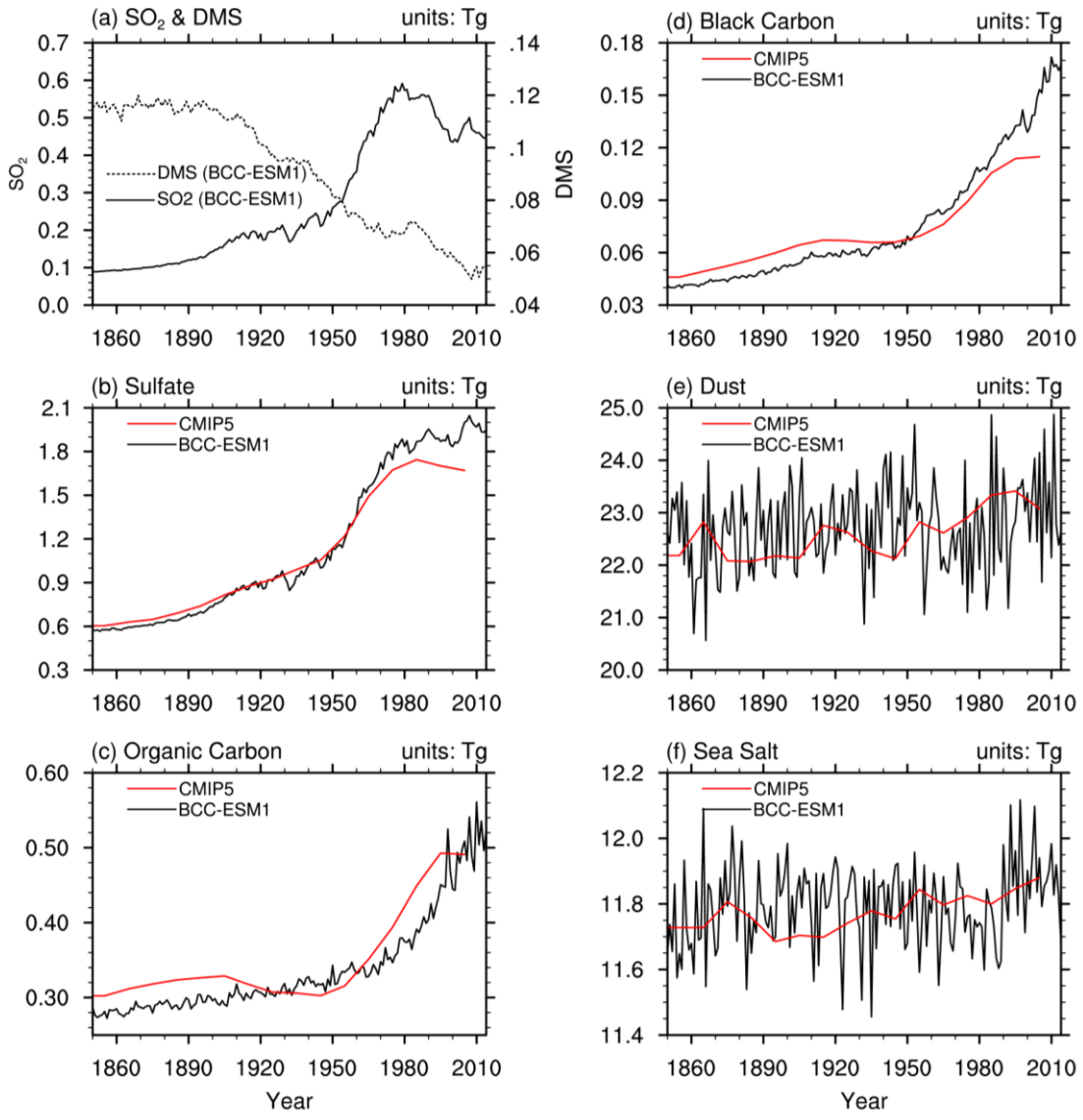


Figure 7. The time series of global yearly amounts of (a) $SO_2$ and DMS and (b-f) aerosols in the whole atmosphere column from the CMIP6 historical simulations of BCC-ESM1 (black lines) and the CMIP5-recommended aerosols masses (red lines). The yearly CMIP5 data are interpolated from the time series in 10-year interval. Units: Tg.

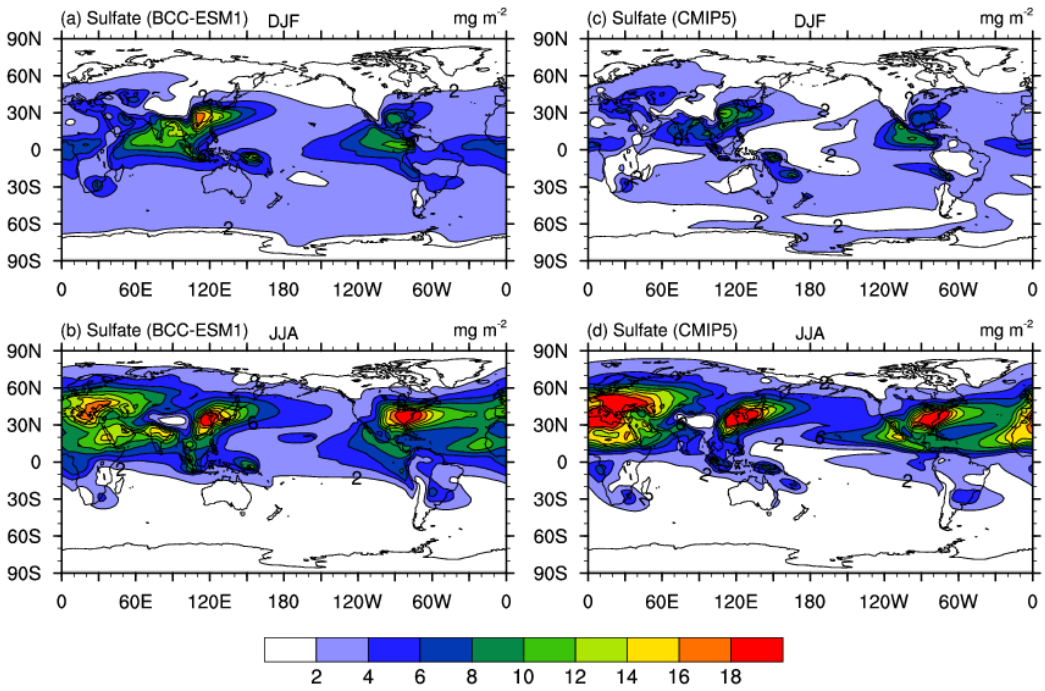


Figure 8. December-January-February (DJF; top panels) and June-July-August (JJA; bottom panels) mean sulfate ($SO_4^{2-}$) aerosol column mass concentrations averaged for the period of 1971-2000. Left panels show the historical simulations of BCC-ESM1, and right panels the CMIP5-recommended data. Units: $mg.m^{-2}$.

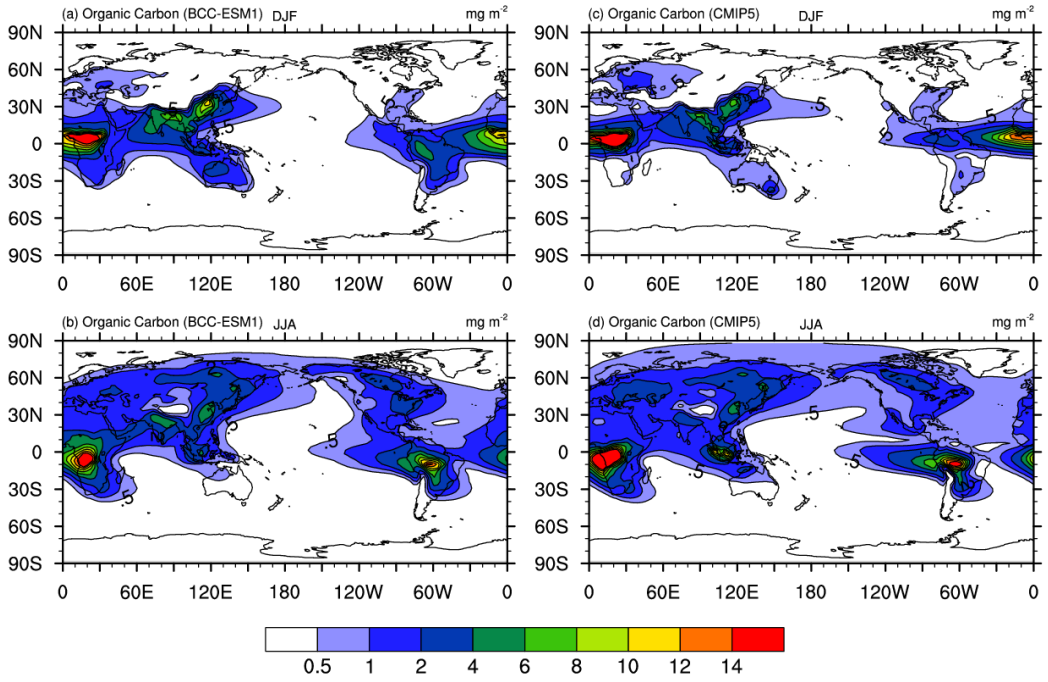


Figure 9. The same as in Figure 8, but for organic carbon (OC) aerosol column mass concentrations. Units: mg $m^{-2}$.

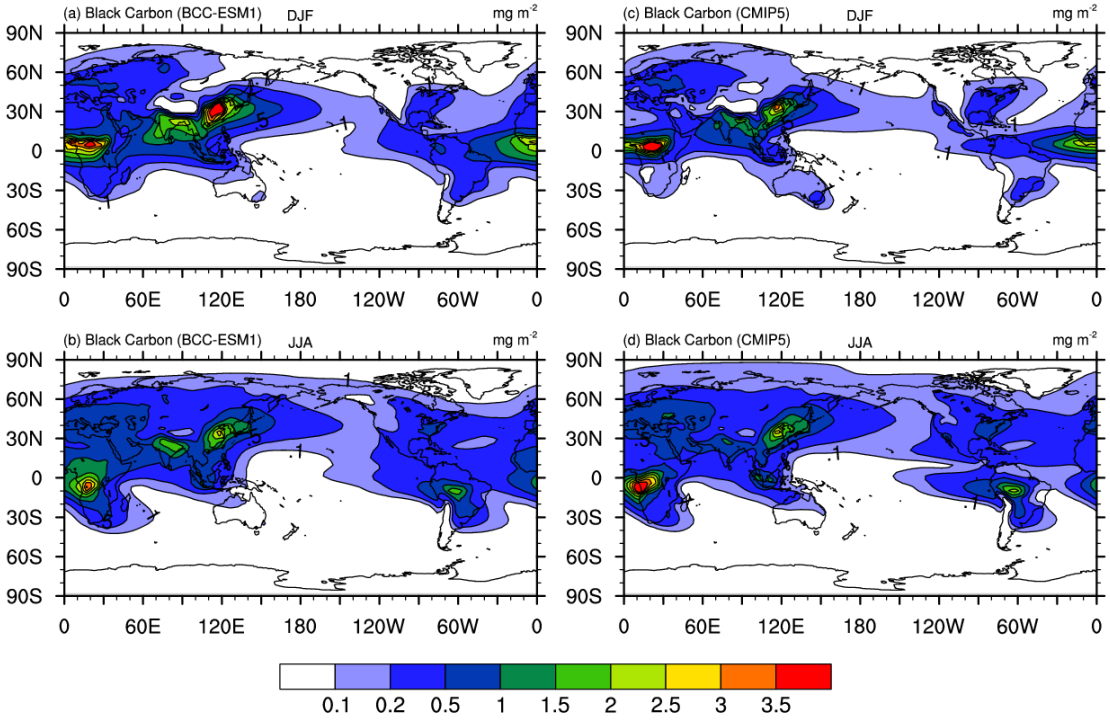


Figure 10. The same as in Figure 8, but for black carbon (BC) aerosol. Units: $mg.m^{-2}$.

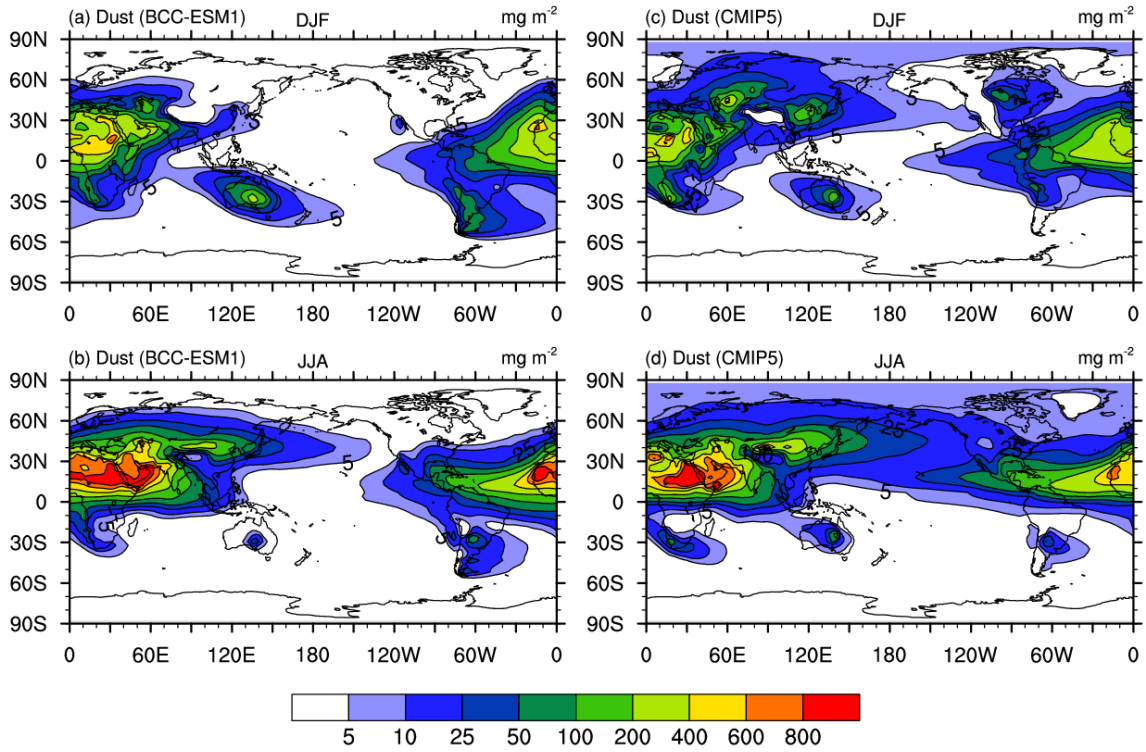


Figure 11. The same as in Figure 8, but for dust aerosol. Units: $mg.m^{-2}$.

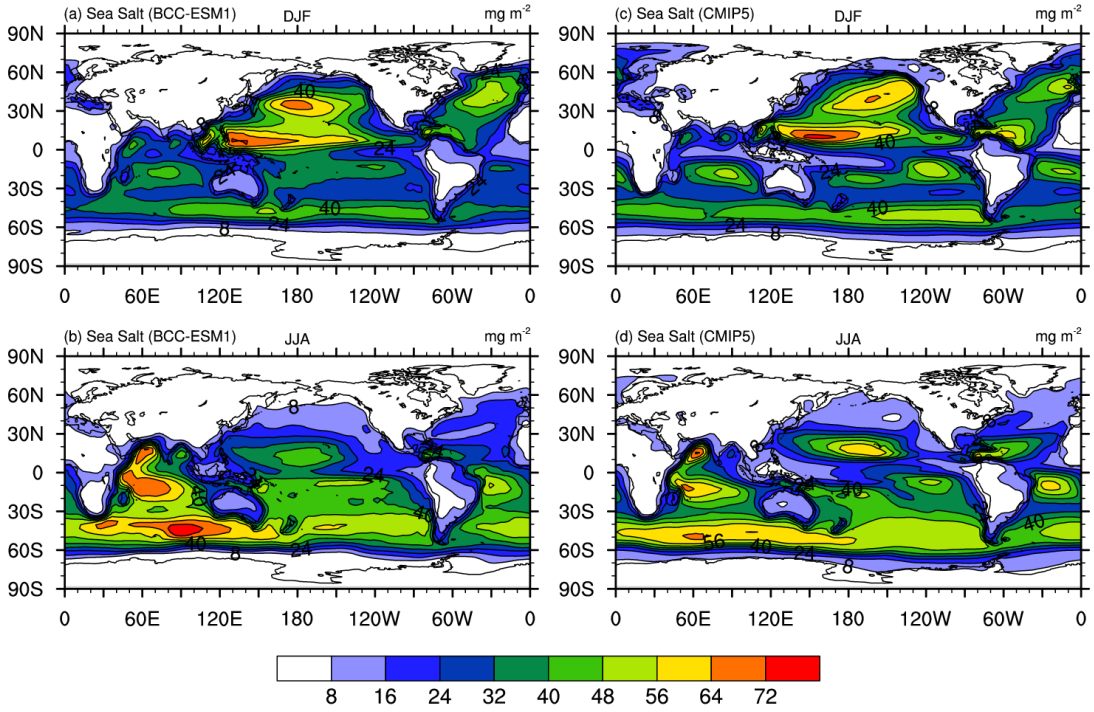


Figure 12. The same as in Figure 8, but for sea salt (SSLT) aerosol. Units: mg.m$^{-2}$.

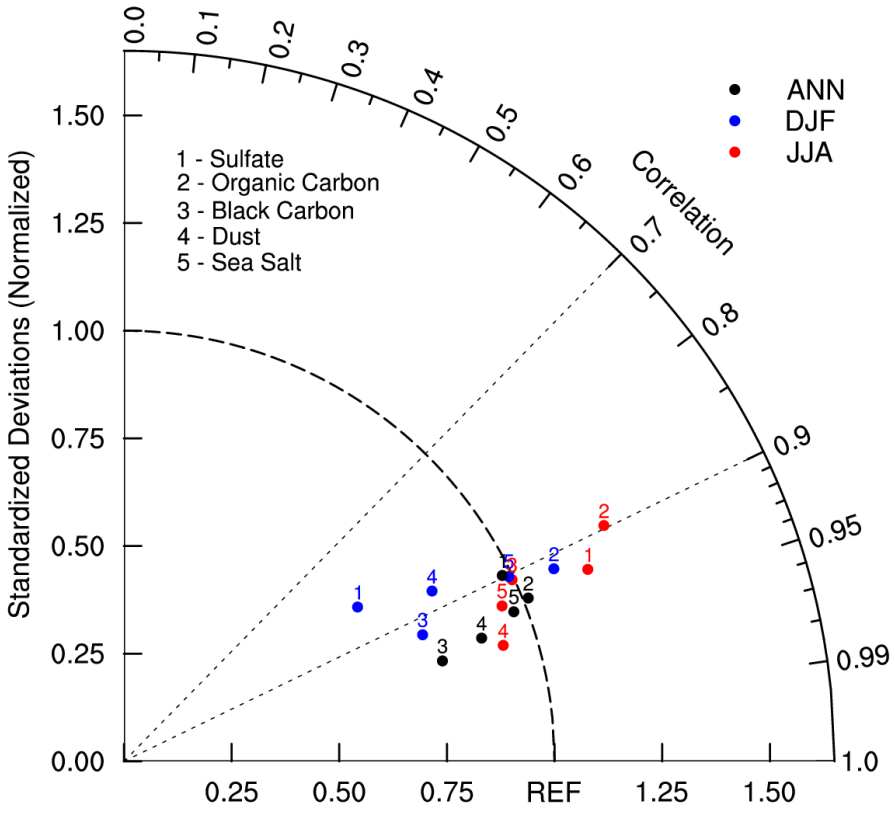


Figure 13. Taylor diagram for the global aerosols climatology (1971–2000) of sulfate, organic carbon, black carbon, dust, and sea salt averaged for December-January-February (DJF), June-July-August (JJA), and annual respectively. The radial coordinate shows the standard deviation of the spatial pattern, normalized by the observed standard deviation. The azimuthal variable shows the correlation of the modelled spatial pattern with the observed spatial pattern. Analysis is for the whole globe. The reference dataset is CMIP5-prescribed dataset.

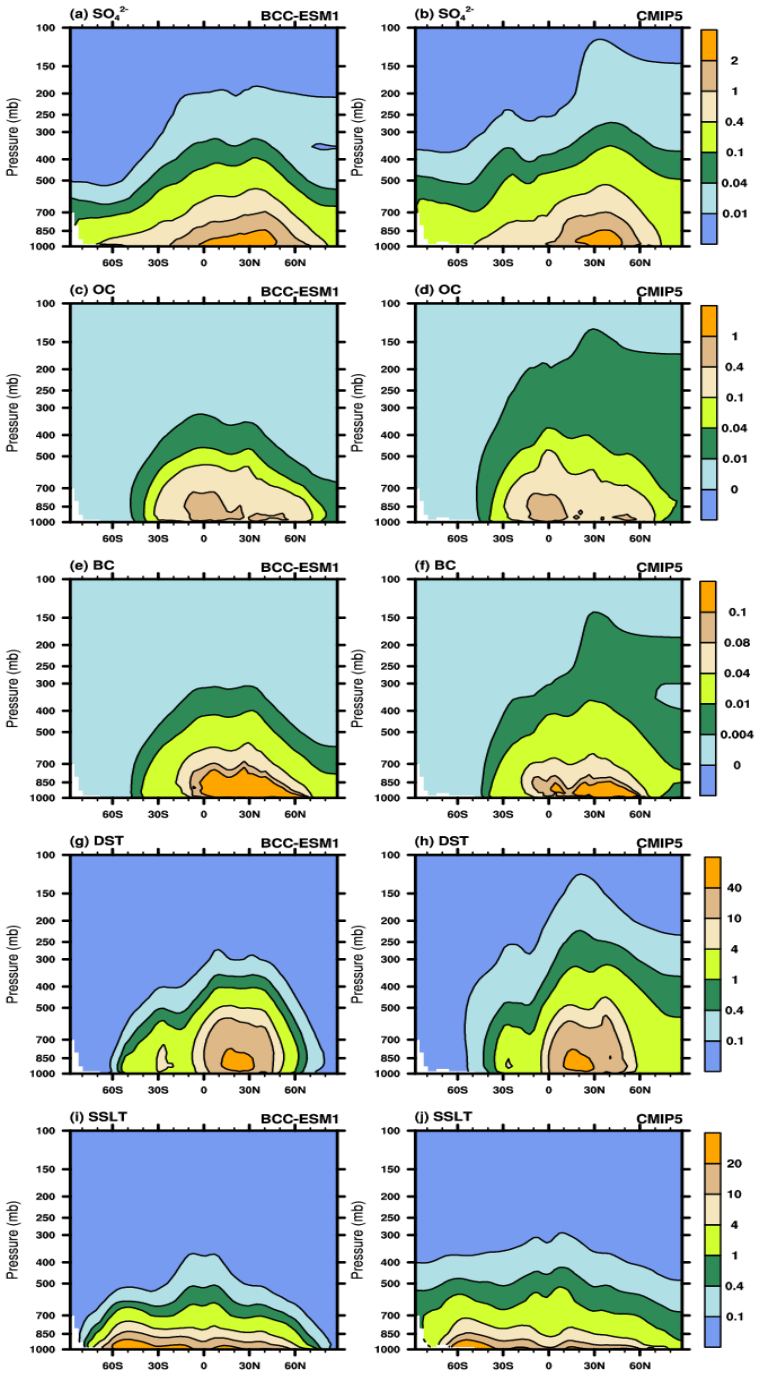


Figure 14. Latitude-pressure distributions of zonally-averaged annual mean sulfate, organic carbon, black carbon, dust, and sea salt aerosol concentrations for the period of 1971-2000. Left panels show the CMIP6 historical simulation of BCC-ESM1, and right panels the CMIP5 recommendation data. Units: μg $m^{-3}$.

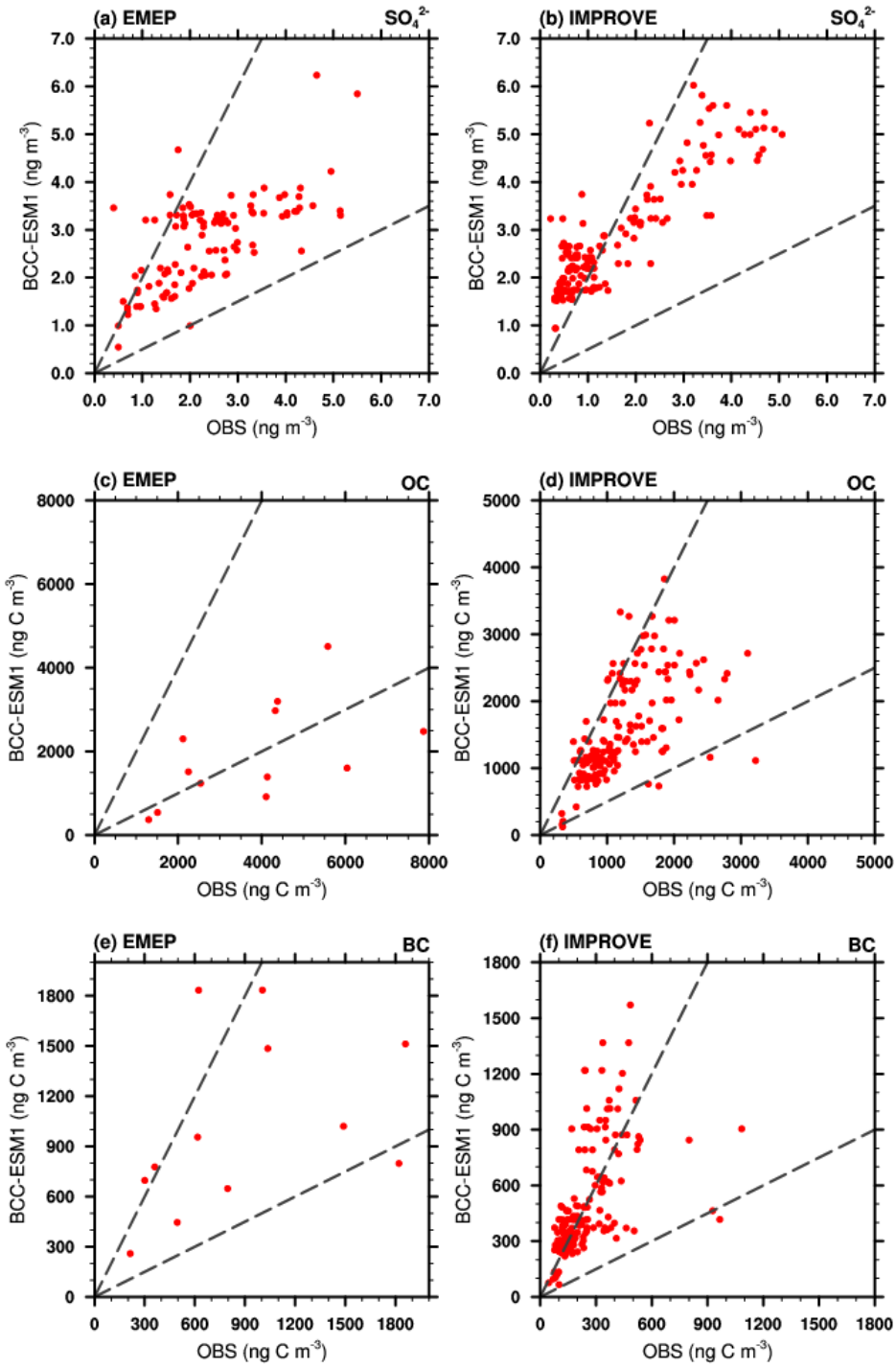


Figure 15. Scatter plots showing observed versus simulated multi-years averaged annual mean sulfate ($SO_4^{2-}$), organic carbon (OC), black carbon (BC) mixing ratios at IMPROVE and EMEP network sites. Observations are averages over the available years 1990–2005 for IMPROVE sites, and 1995–2005 for EMEP sites. Simulated values are those at the lowest layer of BCC-ESM1.

Table 7. Observed versus simulated concentrations of sulfate ($SO_4^{2-}$), organic carbon (OC), black carbon (BC) for the regional mean and spatial standard deviation, minimum and maximum values at HIPPO aircraft observations (BC only), IMPROVE and EMEP network sites, and the spatial correlation between observed and simulated multi-years averaged annual means. Simulated values are selected for the same locations and same valid observation time. The data used same as those in Figure 12.

| | **EMEP** | | | **IMPROVE** | | | **HIPPO** |
|---|---|---|---|---|---|---|---|
| | **$SO4^{2-}$ (Obs/Model)** | **OC (OBS/Model)** | **BC (OBS/Model)** | **$SO4^{2-}$ (OBS/Model)** | **OC (OBS/Model)** | **BC (OBS/Model)** | **BC （OBS/Model）** |
| **Mean Values** | 2.37/2.74 | 3844/1919 | 884/1022 | 1.53/2.79 | 1215/1565 | 249/504 | 8.2/11.1 |
| **Std Deviation** | 1.16/0.93 | 1997/1215 | 572/526 | 1.30/1.20 | 572/745 | 164/296 | 27.9/21.0 |
| **Min Values** | 0.40/0.55 | 1296/369 | 214/259 | 0.22/0.94 | 322/123 | 45/66 | 0.0025/0.066 |
| **Max Values** | 5.50/6.24 | 7867/4510 | 1859/1834 | 5.07/6.02 | 3219/3827 | 1084/1570 | 558.91/267.11 |
| **Correlation (Obs and Model)** | 0.67 | 0.56 | 0.40 | 0.90 | 0.63 | 0.55 | 0.51 |

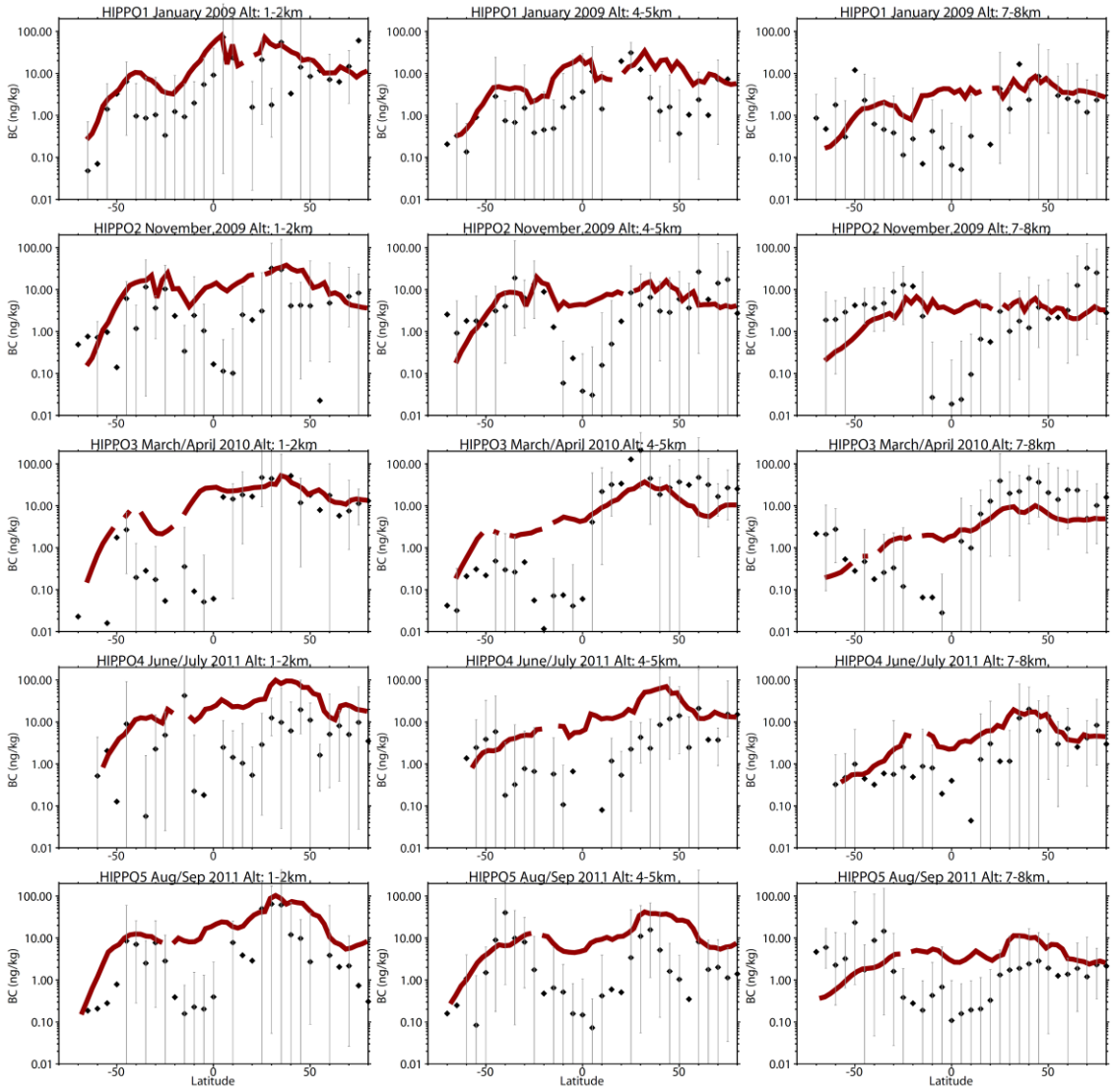


Figure 16. Comparison of modelled black carbon (BC) aerosol (red lines) with observations from HIPPO aircraft campaigns over the Pacific Ocean (black symbols, bars represent the full data range). Observations from different HIPPO campaigns were averaged over 5 °latitude bins and three different altitude bands (left column: 1-2 km, middle column: 4-5 km, and right column: 7-8 km) along the flight track over the Pacific Ocean. Model results were sampled along the flight track and then averaged over the abovementioned regions for comparison.

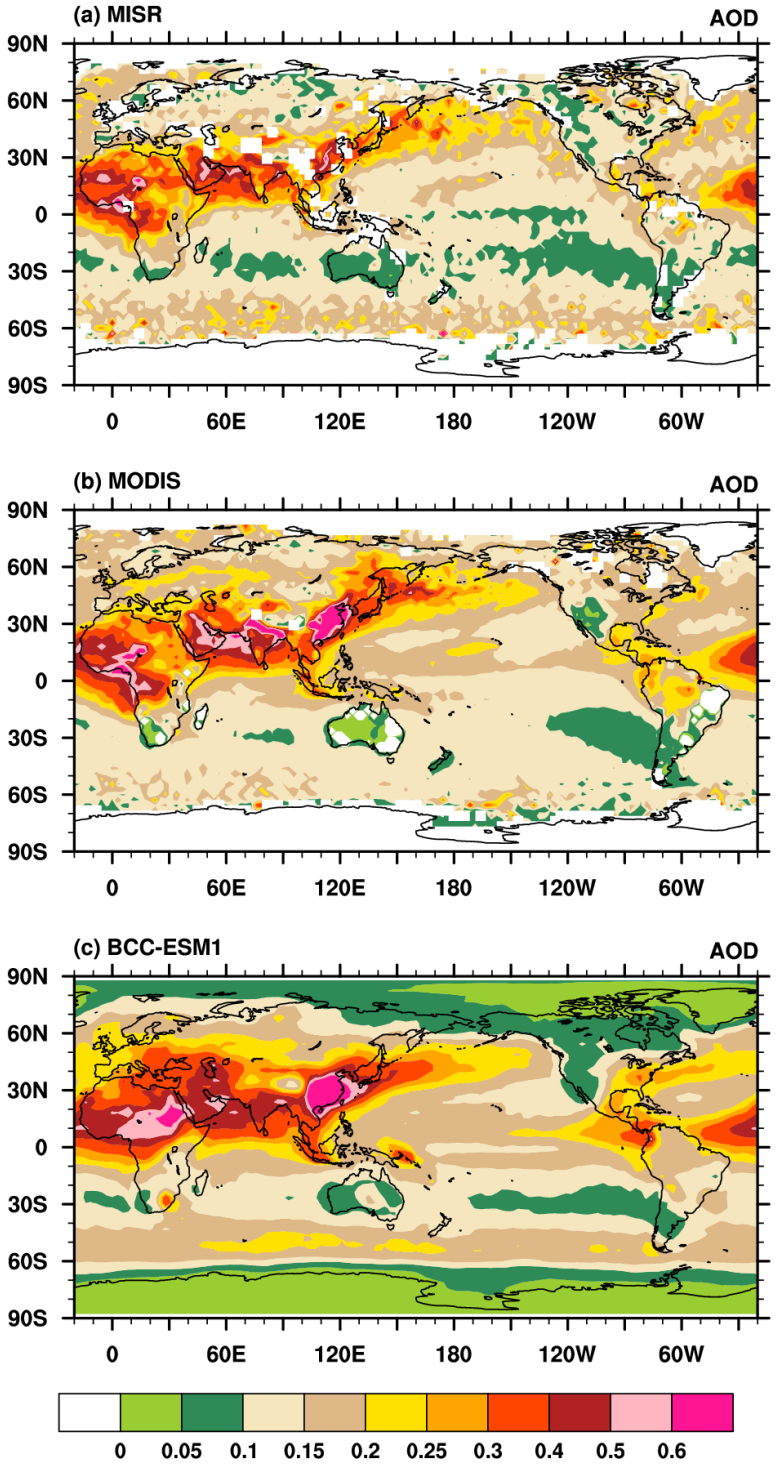


Figure 17. Global distribution of annual mean AOD simulated in BCC-ESM1 compared with the MISR and MODIS data for the year 2008.

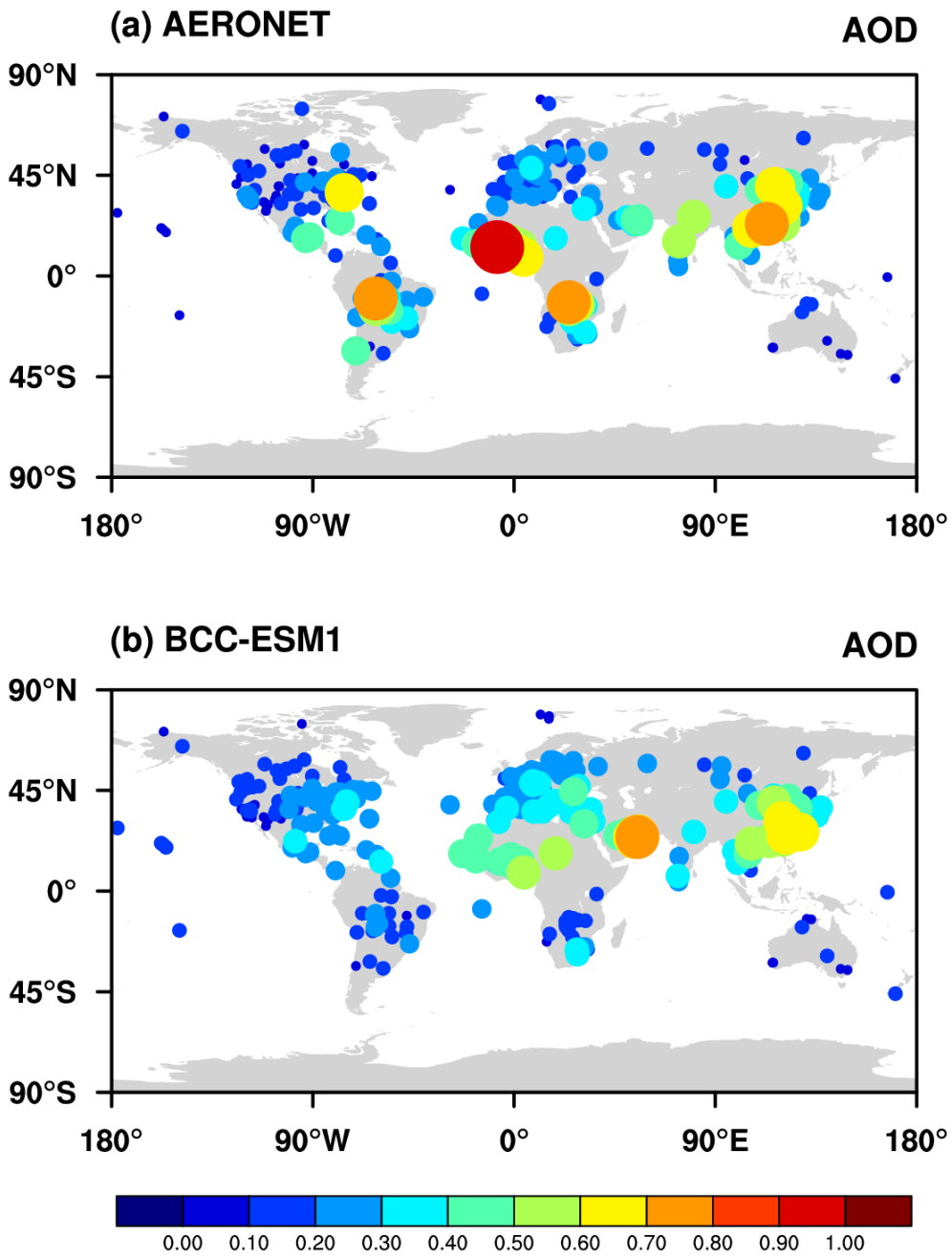


Figure 18. Observed versus simulated annual means of AOD at AERONET sites. Each data point represents the mean averaged for available monthly values of AOD. The dot sizes denote the magnitudes of AOD at sites. The spatial correlation is 0.56.

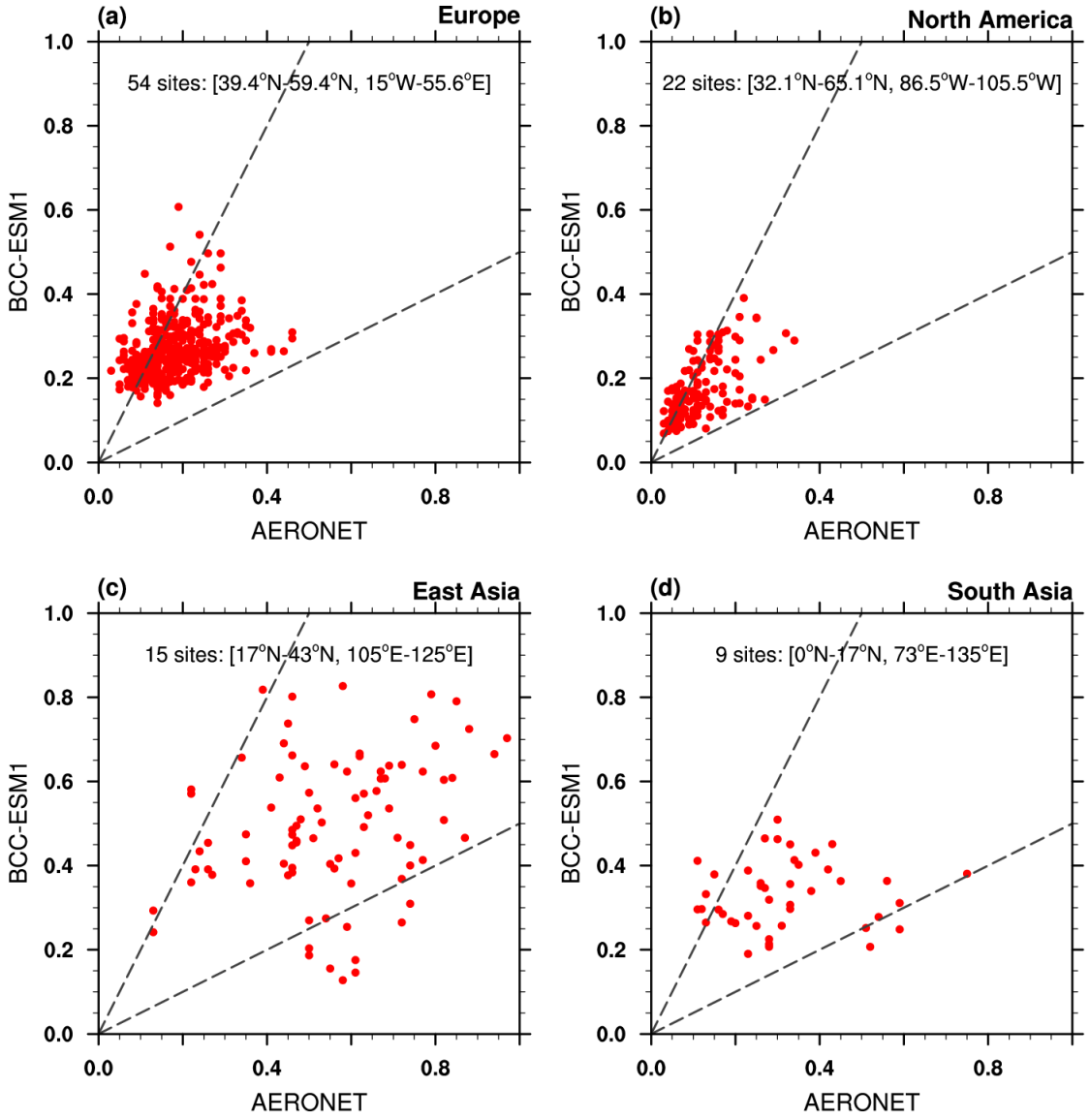


Figure 19. Scatter plots of observed versus simulated monthly mean AOD at AERONET sites in Europe, North America, East Asia, and South Asia over the period of 1998-2005.